



## OPEN Design, synthesis, and optimization of a novel ternary photocatalyst for degradation of cephalexin antibiotic in aqueous solutions

Zeynab Abdeyazdan, Mohammad Rahmati, Arjomand Mehrabani-Zeinabad & Masoud Habibi Zare✉

The widespread use of antibiotics in veterinary and medical applications has increased the possibility of water contamination, which causes adverse effects such as increased bacterial resistance in humans and other organisms. This study, investigates the efficient removal of cephalexin (CPX) using Fe doped  $\text{TiO}_2\text{-Bi}_2\text{O}_3$  nanocomposite, synthesized via the simple sol–gel method as a visible active photocatalyst. The weight fraction of Fe (3–7 wt%), and  $\text{Bi}_2\text{O}_3$  (7–11 wt%) was optimized. The Fe– $\text{TiO}_2\text{-Bi}_2\text{O}_3$  nanocomposite with a weight fraction of 3 and 11% for Fe and  $\text{Bi}_2\text{O}_3$  has the best photocatalytic activity for Cephalexin degradation. The characteristics of photocatalyst with optimum composite (3 wt% of Fe and 11 wt%  $\text{Bi}_2\text{O}_3$ ) were also investigated by X-ray diffraction (XRD), field emission scanning electron microscopy (FESEM), diffuse reflectance spectra (DRS) and FTIR. The DRS spectra approved that the adsorption wavelength of Fe-doped  $\text{TiO}_2\text{-Bi}_2\text{O}_3$  is in the visible light range. The influence of amount of catalyst (0.5–1.5 g/L), Cephalexin concentration (5–15 mg/L) and initial pH of the solution (3–9) in on CPX photodegradation was modeled and optimized using central composite design based on response surface methodology. Maximum cephalexin degradation Under visible light irradiation (50 W LED, 395–400 nm) was achieved about 74% at 5 mg/L of CPX, 1.5 g/L catalyst loading and pH of 9 in 240 min. Moreover, using a 15W UV lamp under the same conditions increased the degradation efficiency to 96% at 120 min. Considering the high potential of Fe– $\text{TiO}_2\text{/Bi}_2\text{O}_3$  nanocomposite in removing Cephalexin antibiotics, it can be considered a suitable candidate for removing antibiotics from contaminated water sources.

**Keywords** Cephalexin, Fe– $\text{TiO}_2\text{/Bi}_2\text{O}_3$ , Photocatalysis, Response surface methodology, Visible light

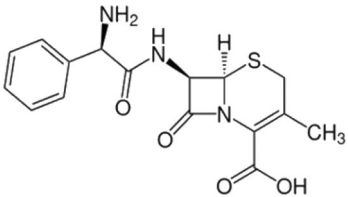
Water contaminations by pharmaceutical compounds has been an environmentally concerning issue in recent years<sup>1,2</sup>. These contaminants, especially antibiotics, enter the environment through various sources, including pharmaceutical industry effluent, hospital wastewater, improper drug disposal, sewage treatment plants, landfill leachate, animal excrement, and agricultural runoff<sup>3,4</sup>. The chemical structure of antibiotics typically includes quinolone groups, sulfonamides, piperazine moieties, and benzene rings, which are recognized as hazardous, toxic, and recalcitrant compounds in the environment<sup>5</sup>. Further, the accumulation of antibiotics in water, because of their long half-life time, can result in the development of antibiotic-resistant bacteria and the dissemination of antibiotic-resistant genes in humans and other living organisms and reduce the effectiveness of the medicine in treating diseases continuously<sup>3,6</sup>. Antibiotics are poorly absorbed in the body, and approximately 50–90% are excreted in the environment. since it is estimated that 100,000 to 200,000 tons of antibiotics are consumed worldwide and are expected to double by 2030, Therefore, the removal of these antibiotics is still challenging<sup>1,7–9</sup>. Cephalexin is a cephalosporin antibiotic, is effective in treating various infectious diseases, such as respiratory infections, middle ear infections, skin infections, and joint infections<sup>10,11</sup>. The presence of these antibiotics in drinking water can lead to various health issues, including headaches, nausea, vomiting<sup>12</sup> and in cases of high concentrations, may lead to serious complications such as acute kidney failure, elevated liver

Department of Chemical Engineering, Isfahan University of Technology, Isfahan 84156-83111, Iran. ✉email: masoud.habibi@ce.iut.ac.ir

enzymes, and thrombocytopenia. The removal of these antibiotics from the environment is essential to maintain public health and prevent their adverse effects on human health<sup>10,13</sup>. Various physical, biological, and chemical methods have been proposed to remove all kinds of antibiotics and pollution from water environments<sup>14–22</sup>. Each of method has its own advantages and shortcomings, which typically hinder their exclusive application<sup>23</sup>. For instance, conventional physical methods remove pollutants from wastewater by transferring them to another phase. However, this process generates hazardous secondary solid waste, requiring additional treatment measures<sup>9,24</sup>. Biological methods often exhibit limited efficiency due to the presence of stable naphthol rings as the main structural feature in pharmaceutical compounds, their toxicity to microorganisms, and their low biodegradability. Additionally, they require a high hydraulic retention time and special operating conditions to continue microorganism metabolism, leading to the production of a large amount of sludge<sup>25,26</sup>. Nowadays, advanced oxidation processes, specifically photocatalytic processes have been considered as effective method for decomposition of emerging pollutants into non-toxic by-products with ability of using solar energy. The advantages of photocatalysis are that it is operation under ambient temperature and pressure, mineralization of organic pollutants, economic, environmentally friendly, sustainability (use of solar light) and the ease of operation ability<sup>27–32</sup>. Photocatalytic processes consist of four stages: absorption of light energy exceeding the semiconductor's bandgap to generate electron–hole pairs in the conduction and valence bands, charge separation, transfer to the catalyst surface, and the formation of reactive species such as superoxide and hydroxyl radicals, that own the power to attack pollutant molecules and degrade them to harmless compounds and simpler intermediates<sup>33–35</sup>. Titanium dioxide is the most commonly used semiconductor in photocatalytic degradation of organic compounds due to its excellent optical properties, chemical resistance, strong oxidizing power, and low cost and toxicity.  $\text{TiO}_2$  cannot function effectively due to its large band gap of 3.4 eV which limits the absorption to UV region and rapid recombination rate of the photo generated  $e^-/h^+$  pairs. A wider bandgap limits electron excitation to UV light ( $\sim 5\%$  of solar energy)<sup>36,37</sup>. Many techniques, including surface remodeling to increase the active catalytic area, structure design of the semiconductor matrix, surface sensitization, metal or nonmetal doping, and heterostructure production and composite have been used to lower electron–hole pair recombination and enhance charge separation efficiency. Collectively, these approaches not only boost overall photocatalytic activity but also shift the operational response from the ultraviolet into the visible light range<sup>38–42</sup>. Doping of semiconductor materials can significantly alter the characteristics of the intrinsic semiconductors. Many studies have focused on enhancing  $\text{TiO}_2$  photocatalytic performance by noble metal deposition, metal doping, or nonmetal ion incorporation<sup>43–47</sup>. Doping Fe can operate as a surface trap and can not only reduce the band gap of  $\text{TiO}_2$  but also enhance its light response and utilization efficiency<sup>48</sup>. Research has been shown that doping with  $\text{Fe}^{3+}$  improves photocatalytic activity<sup>49,50</sup> and light absorption is transferred to Visible region<sup>51</sup>. For instance, Swati Sood<sup>52</sup> experimentally confirmed that  $\text{Fe}^{3+}$  doping reduces the band gap of  $\text{TiO}_2$  from 3.2 to 2.1–2.5 eV, improves the light energy utilization and enhances photocatalytic performance. Furthermore, the similarity in radius between  $\text{Fe}^{3+}$  (0.064 nm) and  $\text{Ti}^{4+}$  (0.068 nm) allowed  $\text{Fe}^{3+}$  to infiltrate the lattice of  $\text{TiO}_2$  and serve as a trapping center. Yajun Yang<sup>53</sup> investigated the effect of  $\text{Fe}^{3+}$  doping on the grain growth of  $\text{TiO}_2$  and the morphology of  $\text{Fe}^{3+}$  as well as the transformation and phase transition of the existing morphology in the process, and the results showed that  $\text{Fe}^{3+}$  can replace  $\text{Ti}^{4+}$  and has good electrocatalytic activity for the reduction of  $\text{CO}_2$  and  $\text{H}_2\text{O}$  to  $\text{CH}_4$ . In another study, Ellouzi et al.<sup>54</sup> synthesized iron-doped  $\text{TiO}_2$  nanoparticles with different molar ratios of iron, i.e., 0.1% and 0.2%, by coprecipitation method. Their results showed that the photocatalysts were well crystallized mainly in the anatase phase and the optical properties of the powders changed from UV to the beginning of the visible light (Vis-L) region. Fe doping markedly enhanced the photocatalytic degradation of methyl orange, with the 0.2% doped sample achieving a 4.2-fold improvement over pure  $\text{TiO}_2$ , underscoring the importance of Fe content in optimizing photocatalytic performance. Additionally, iron is abundant in nature, cost-effective, and environmentally benign. The magnetic properties of iron play a crucial role in recovering the used catalyst from the solution, facilitating practical applications of the photocatalyst, making it a more suitable modifier for photocatalysts<sup>55,56</sup>. In this study,  $\text{Fe}^{3+}$  was selected as a dopant for  $\text{TiO}_2$  due to its compatible ionic radius and ability to enhance photocatalytic performance. Moreover, the combination of semiconductors generates significant synergistic effects. The benefits of using associations of semiconductors are twofold: (1) to extend the photoresponse by coupling a large band gap semiconductor with a narrower bandgap semiconductor, and (2) to reduce the recombination rate of photogenerated charge carriers<sup>57</sup>. Due to its low band gap (2.8–2.58 eV), non-toxicity, and ease of synthesis,  $\text{Bi}_2\text{O}_3$  is an appropriate oxide for the development of nanocomposites with  $\text{TiO}_2$ <sup>58,59</sup>. Additionally, with  $\text{Bi}_2\text{O}_3$  being a p-type and  $\text{TiO}_2$  an n-type semiconductor, one acts as an electron donor while the other functions as an electron acceptor<sup>60,61</sup>. The formation of a  $\text{TiO}_2/\text{Bi}_2\text{O}_3$  heterostructure enhances the separation of redox reaction sites and preserves the strong redox capacity of the carriers. This not only reduces the recombination rate of electron–hole pairs but also shifts the  $\text{TiO}_2$  band gap into the visible light range through the photosensitizing effect of  $\text{Bi}_2\text{O}_3$ , thereby enhancing the photocatalytic activity of the hybrid material<sup>62,63</sup>. Mingjun Wang et al.<sup>64</sup> synthesized nano-flower  $\beta\text{-Bi}_2\text{O}_3/\text{TiO}_2$  composites via a solvothermal method and evaluated their photocatalytic performance based on the Bi/Ti molar ratio. They prove formation of a staggered heterojunction enhanced charge carrier separation, significantly improve Rhodamine B degradation efficiency from 61.2 to 99.6% at a Bi/Ti ratio of 2.1%. Thier results underscore the potential of  $\text{Bi}_2\text{O}_3/\text{TiO}_2$  composites for advanced photocatalytic applications. Ruiz et al.<sup>65</sup> synthesized a series of  $\text{TiO}_2$ -modified  $\text{Bi}_2\text{O}_3$  photocatalysts with varying  $\text{TiO}_2$  content via an in situ hydrothermal process. Their evaluation of photocatalytic performance for the degradation of methyl orange (MO) and methylene blue (MB) revealed that these composites significantly outperformed the pure  $\text{TiO}_2$  and  $\text{Bi}_2\text{O}_3$ . Notably, the  $\text{BiT}_{16}$  sample achieved degradation efficiencies of approximately 93.9% for MO and 98.2% for MB within 120 min at 30 ppm. This remarkable activity is attributed to the optimized band gap, enhanced textural characteristics, effective  $\text{TiO}_2$  integration, and a reduction in electron–hole recombination. Sood et al.<sup>66</sup> synthesized and characterized  $\text{Bi}_2\text{O}_3/\text{TiO}_2$  catalyst and its performance on degradation of the ofloxacin antibiotic

Name of the chemical	Chemical formula	Purity (%)	Manufacturer
Tetra butyl ortho-titanate (TBOT)	$C_{16}H_{36}O_4Ti$	99.99	Merck
Ethanol	$C_2H_5OH$	99.5	Sigma Aldrich
Iron (III) nitrate 9 water	$Fe(NO_3)_3 \cdot 9H_2O$	99.99	Merck
Bismuth nitrate 5 water	$Bi(NO_3)_3 \cdot 5H_2O$	99.99	Merck
Cephalexin	$C_{16}H_{17}N_3O_4S$	99	Merck
Sodium hydroxide	NaOH	95	Sigma Aldrich
Hydrochloric acid	HCl	37	Merck

**Table 1.** List of chemicals used to conduct experiments.

Drug brand	Keflex
Chemical formula	$C_{16}H_{17}N_3O_4S$
Chemical structure	
Solubility (mg/L)	1790
Molecular weight (g/mol)	347.39
pKa	6.88–2.56

**Table 2.** Physical, chemical and molecular structure characteristics of cephalexin.

under sunlight radiation. By increasing the ratio of Bi/Ti from 1 to 10%, the degradation efficiency of the pollutant was increased from 30 to 92% under operating conditions of pH = 7, catalyst concentration 0.5 g/L, pollutant concentration 25 mg/L and processing time of 120 min. The energy gap of pure titanium dioxide was 3.16 eV, but it was lowered to 3.06 eV by using the ideal Bi/Ti ratio of 10%, which had a substantial effect on the ability to absorb light in the visible range. Bismuth-based semiconductors exhibit low bandgaps and strong photocatalytic activity due to the hybridization of the 6s2 orbitals of  $Bi^{3+}$  with the O 2p orbitals, which creates a new valence band and reduces the bandgap<sup>67</sup>. For these reasons, bismuth titanate exhibits excellent photocatalytic efficiency for the removal of organic pollutants by limiting  $e^-/h^+$  recombination and facilitating photocatalytic reactions. This study investigates the removal of the pharmaceutical pollutant cephalexin from aquatic environments due to its potential adverse effects on water quality and ecosystem health. For the first time, an iron-based catalyst doped with titanium dioxide and coupled with bismuth oxide was synthesized to evaluate its performance in the photocatalytic degradation of cephalexin. The synthesized nanocatalyst demonstrated enhanced degradation efficiency, reduced energy consumption, and potential for recyclability. The photocatalysts were fabricated using the sol–gel method and comprehensively characterized via X-ray diffraction (XRD), energy-dispersive X-ray spectroscopy (EDX), field emission scanning electron microscopy (FE-SEM), and Fourier transform infrared spectroscopy (FTIR). Key operational parameters, including the initial concentration of cephalexin, solution pH, and photocatalyst dosage, were systematically optimized using response surface methodology (RSM) to achieve maximum degradation efficiency.

## Experimental methods

### Materials and equipment

In this study,  $TiO_2$  nanoparticles were synthesized via a sol–gel method using tetrabutyl orthotitanate (TBOT) as the precursor and ethanol as the solvent. Iron (III) nitrate nonahydrate ( $Fe(NO_3)_3 \cdot 9H_2O$ ) and Bismuth(III) nitrate pentahydrate ( $Bi(NO_3)_3 \cdot 5H_2O$ ) were used as the precursors of the iron ion and bismuth oxide to modify  $TiO_2$ , respectively. Hydrochloric acid (HCl) and sodium hydroxide (NaOH) were used to adjust the pH solution and were obtained from Merck and Sigma Aldrich. Table 1 shows the materials used in the study, while Table 2 presents the physical and chemical properties and molecular structure of cephalexin. Table 3 presents the test equipment used and its parameters.

### Synthesis of Fe-doped $TiO_2/Bi_2O_3$ nanocatalyst

The Fe– $TiO_2/Bi_2O_3$  nanocatalysts with varying weight percentages of  $Fe^{3+}/Ti^{4+}$  and  $Bi_2O_3/TiO_2$  (as presented in Table 4) were synthesized using the sol–gel method. Initially, amounts of iron nitrate salts in 5 mL and bismuth nitrate in 10 mL of ethanol were dissolved under ultrasonic waves for 20 and 120 min, respectively. Iron nitrate salt solution and 2.5 mL of tetrabutyl orthotitanate were simultaneously added drop by drop to the flask containing 25 mL of ethanol. In the next step, for adjusting of the pH, 2 drops of 37% hydrochloric acid were added to the solution and stirred for 2 h. Then a bismuth nitrate salt solution with pH of 1 was added to

Equipment	Model	Manufacturer
Digital scale	Of 300	A&D Company
Magnetic-thermal stirrer	HS-860	Made in Iran
pH meter	SL-901	SANA-India
Ultrasonic bath	PARSONIC 2600s	PARS NAHAND ENGG.Co
Oven	Oven 240-model code 3494	Behdad
UV-visible spectrophotometry	Lambda2S-UV-Vis	Perkin Elmer
Furnace	TMF-2200	Eyela
Centrifuge	Universal 320	Hettich
Mercury thermometer	Zeal England	Made in England
Water pump	AQ202	Made in Iran
Air compressor	AP-320	AQUATEC

**Table 3.** List of laboratory equipment used.

Experiment	Fe <sup>3+</sup> /Ti <sup>4+</sup> (wt ratio)	Fe (NO <sub>3</sub> ) <sub>3</sub> ·9H <sub>2</sub> O (g)	Bi <sub>2</sub> O <sub>3</sub> /TiO <sub>2</sub> (wt ratio)	Bi (NO <sub>3</sub> ) <sub>3</sub> ·5H <sub>2</sub> O (g)
1	0.07	0.178	0.07	0.084
2	0.03	0.076	0.07	0.084
3	0.05	0.127	0.07	0.084
4	0.05	0.127	0.09	0.109
5	0.07	0.178	0.09	0.109
6	0.05	0.127	0.11	0.133
7	0.03	0.076	0.09	0.109
8	0.03	0.076	0.11	0.133
9	0.07	0.178	0.11	0.133

**Table 4.** Amounts of used salts for various weight ratios of Fe<sup>3+</sup>/Ti<sup>4+</sup> and Bi<sub>2</sub>O<sub>3</sub>/TiO<sub>2</sub> in synthesizing of Fe-TiO<sub>2</sub>/Bi<sub>2</sub>O<sub>3</sub> nanocatalysts.

the solution. To enhance hydrolysis and minimize particle size, the solution underwent ultrasonic treatment for an additional 20 min and was then stirred at ambient temperature for 22 h to promote gel formation. Then, the produced gel was dried in the oven at 80 °C for 20 h. Finally, the obtained powders were calcined in an electric furnace at a temperature of 500 °C for a period of 2 h. Figure 1 schematically represents the mentioned stages step by step<sup>22,63</sup>.

### Nanocatalyst characterization

**X-ray diffraction (XRD):** It is a non-destructive analytical technique used to describe the crystal structure of unknown materials. XRD patterns of the produced nanoparticles were acquired using an ASENWARE model AW-XDM300 device utilizing a CO-KA X-ray tube with an input voltage of 40 kV, while 2 $\theta$  changes from 20 to 80 degrees with a step time of 1 s and a step size of 0.05 degrees.

**Field emission scanning electron microscope (FE-SEM):** upon impact of electron beams to a sample, the electrons of the material are excited, and as they return to their original orbit, they are emitted from the sample's surface in the form of an electron beam, which is collected and analyzed by a detector. The sample's reflected rays are utilized to examine the surface morphology. The Quanta FEG-450, made by FEI, USA, was utilized to obtain SEM images and investigate the morphology of composite nanocatalysts.

**UV-VIS diffuse reflectance spectroscopy (UV-VIS DRS):** UV-Vis diffuse reflectance spectroscopy (UV-Vis DRS) was conducted to investigate the optical properties of the synthesized catalysts. In this method, the reflection of light from the catalyst surface is recorded when exposed to ultraviolet and visible light at different wavelengths. This approach can be used to investigate and analyze semiconductors' energy gap and light absorption spectra. The utilized device is the Jasco model V-670, which is made in Japan.

**Fourier transform infrared spectrometer (FT-IR):** infrared spectroscopy has been used as a method to determine the structure and measurement of chemical species and identify organic compounds. It is based on the absorption of radiation and the investigation of vibrational mutations of molecules and polyatomic ions. Functional groups absorb at a certain frequency in the infrared, which is used to assess the presence or absence of one or more distinct functional groups inside a chemical. FT-IR spectra of the produced catalysts were measured using a FT-IR type Tensor 27 from Bruker, Germany.

### Photocatalytic activity

For the photocatalytic degradation of the pollutant in suspension, a double-walled glass reactor with useful volume of 180 mL (height 8.5 cm and diameter 5.2 cm) was used. To maintain a stable reaction temperature, water was circulated through the reactor's outer jacket. Aeration was employed to enhance the concentration

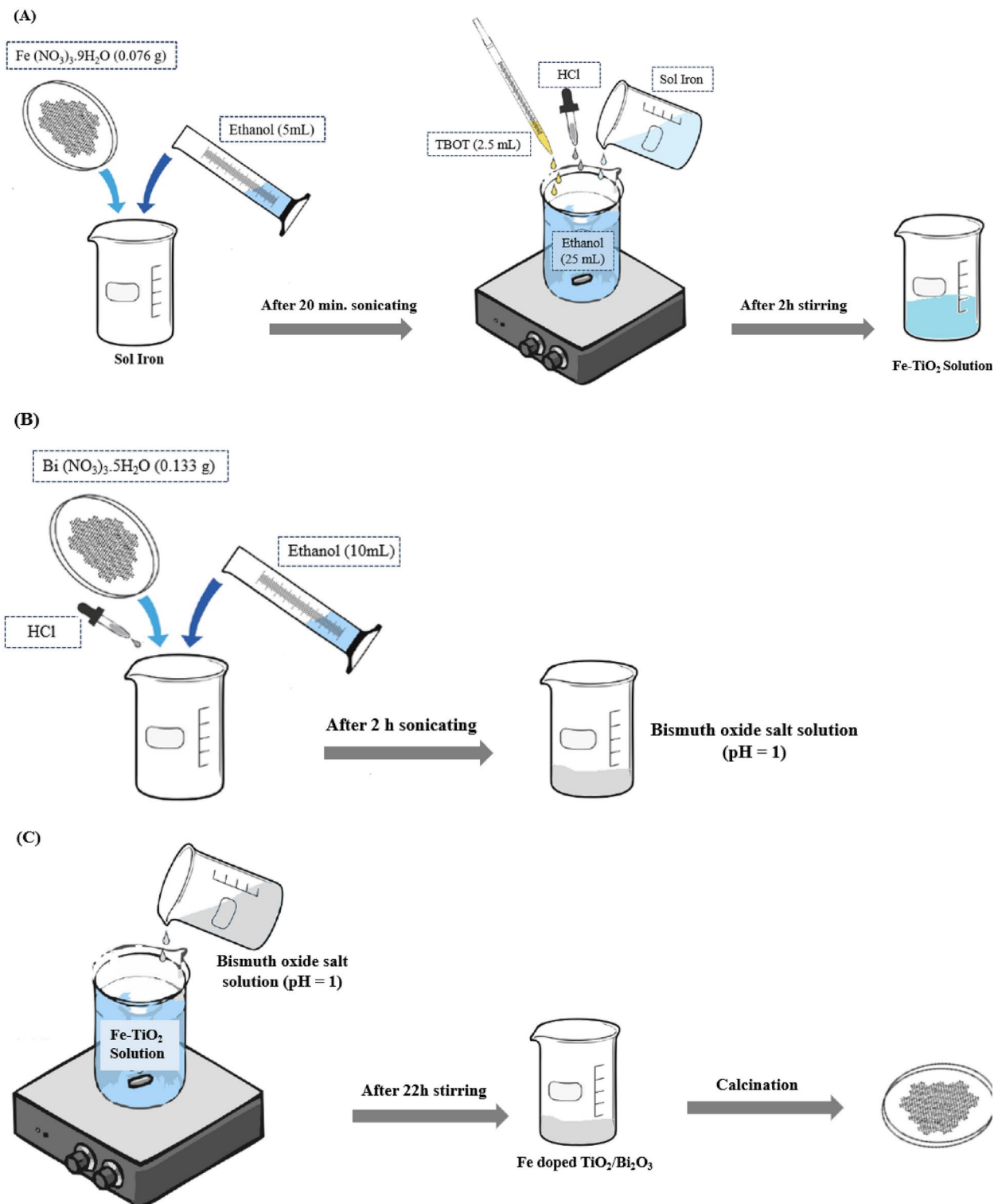


**Fig. 1.** Representation of synthesizing stages of Fe-TiO<sub>2</sub>/Bi<sub>2</sub>O<sub>3</sub> nanocatalyst with weight ratios of  $\text{Fe}^{3+}/\text{Ti}^{4+} = 3$  and  $\text{Bi}_2\text{O}_3/\text{TiO}_2 = 11$ .

of dissolved oxygen, facilitating the generation of hydroxyl radicals necessary for the photocatalytic process. To suspend the nanocatalyst and form uniform concentrations of ingredients a magnetic stirrer was used. A 50-W LED with a maximum absorption wavelength of 400–395 nm and a 15-W moonlight lamp were utilized to produce visible and UV light, respectively. Irradiation was applied at a distance of 15 cm from the reactor top. Figure 2 depicts the experimental scheme of a photoreactor using visible light radiation.



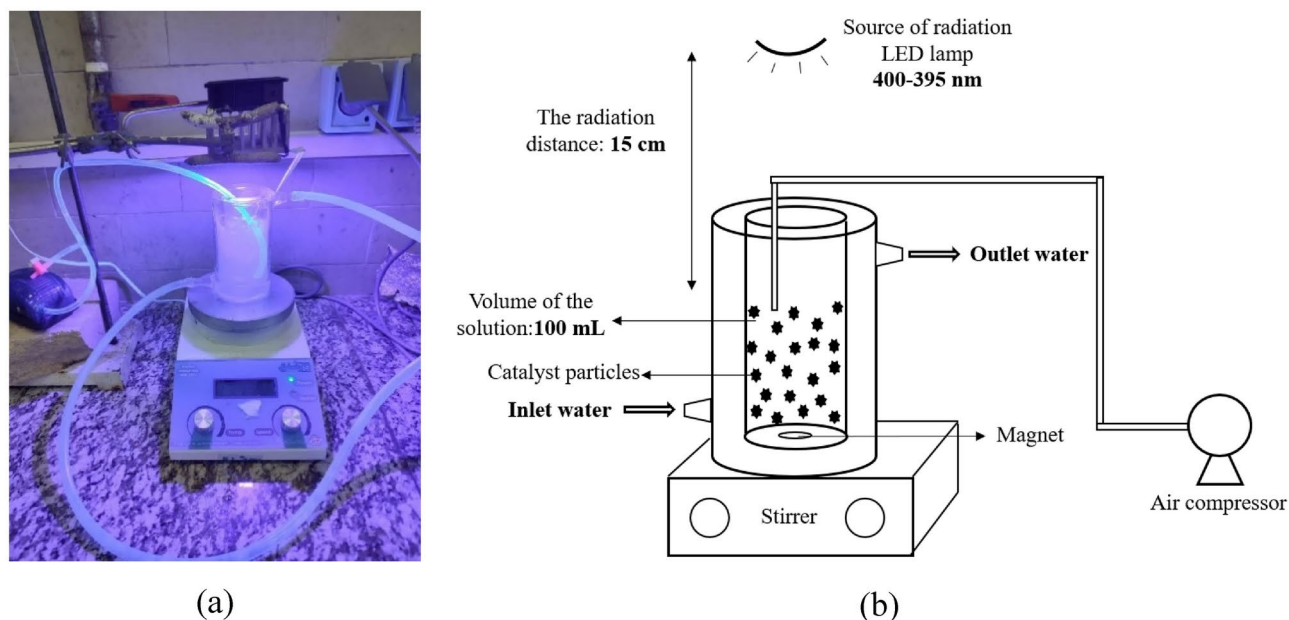


**Fig. 2.** (a) main system (b) laboratory scheme of the photoreactor used with visible light radiation.

In a typical experiment, Fe–TiO<sub>2</sub>/Bi<sub>2</sub>O<sub>3</sub> photocatalyst was dispersed in 100 mL of cephalexin aqueous solution. All experiments are carried out at room temperature. The suspension was stirred in dark conditions for 60 min to achieve adsorption–desorption equilibrium. The duration of light irradiation in all experiments was 240 min. During the irradiation, 4 mL of the suspension was taken out at given time intervals, then centrifuged (5000 rpm, 15 min) to remove the residual photocatalyst powder, and analyzed by a UV–visible spectrophotometer with deionized water as a reference sample. The photocatalytic degradation efficiency was calculated according to Eq. (1).

$$\text{Pollutant removal efficiency} = ((C_0 - C)/C_0) \times 100\% \quad (1)$$

where  $C_0$  and  $C$  are the initial and the final concentrations of cephalexin in the solution.

### Spectrophotometric analysis

In the spectrophotometric method, a calibration curve is prepared to measure an unknown concentration of the pollutant solution. For this purpose, a spectrometer was used to measure the absorbance of a dilute cephalexin solution in the wavelength range of 190–400 nm, and the absorbance was plotted in terms of wavelength as shown in Fig. 3. According to the curved bar, the maximum wavelength ( $\lambda_{\text{max}}$ ) was obtained at 261 nm<sup>68</sup>. To draw this curve, a stock solution with a concentration of 100 mg/L of cephalexin was prepared and based on it, solutions of cephalexin with different concentrations of 0, 5, 10, 15, 20, 25, and 30 mg/L were prepared. The amount of absorption for each of the prepared solutions was measured by a spectrophotometer in the range of the maximum wavelength, and the calibration curve was obtained by drawing the absorption values versus concentration, as shown in Fig. 4.

### Design experiment by response surface method

The traditional method of changing one factor at a time while leaving other features constant necessitates numerous tests in which interactions between parameters are not investigated. As an alternative, design of experiments is a statistical method for investigating the simultaneous influence of multiple characteristics on system response. This strategy utilizes statistical analysis to conduct a subset of experiments rather than a large number of experiments to obtain an accurate scientific result<sup>69</sup>. This not only lowers costs, but also saves time. Today, in the analysis of topics where the desired response is influenced by multiple variables, several statistical methods, such as response surface, are used, which is an efficient method for modeling, evaluating, and improving data<sup>70</sup>.

The Box–Behnken design, the most widely-used form of RSM design, was chosen to assess the effect of three independent factors, initial cephalexin concentration<sup>71,72</sup>, nanocatalyst concentration<sup>73</sup> and pH<sup>74–76</sup>, at three levels of low (–1), medium (0) and high (+1) and their interactions on the response (pollutant degradation efficiency). Design Expert software<sup>®</sup> was used to analyze the results of the experiment. Table 5 provides information about the operating ranges and levels of the independent variables of this study.

The total number of the experimental runs ( $N$ ) was obtained using Eq. (2).

$$N = 2K(K - 1) + C_p \quad (2)$$

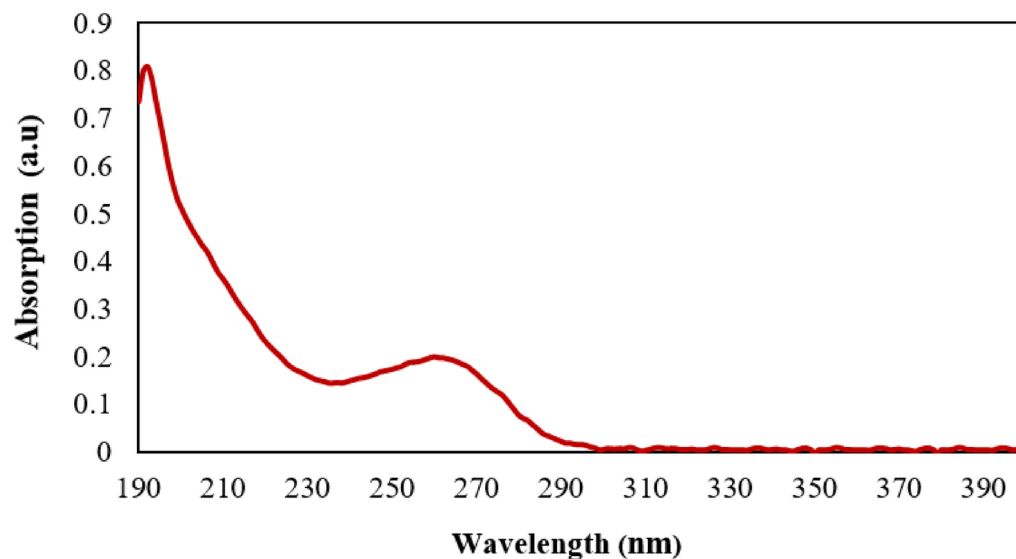


**Fig. 3.** Absorption spectrum of cephalixin to determine the maximum wavelength.

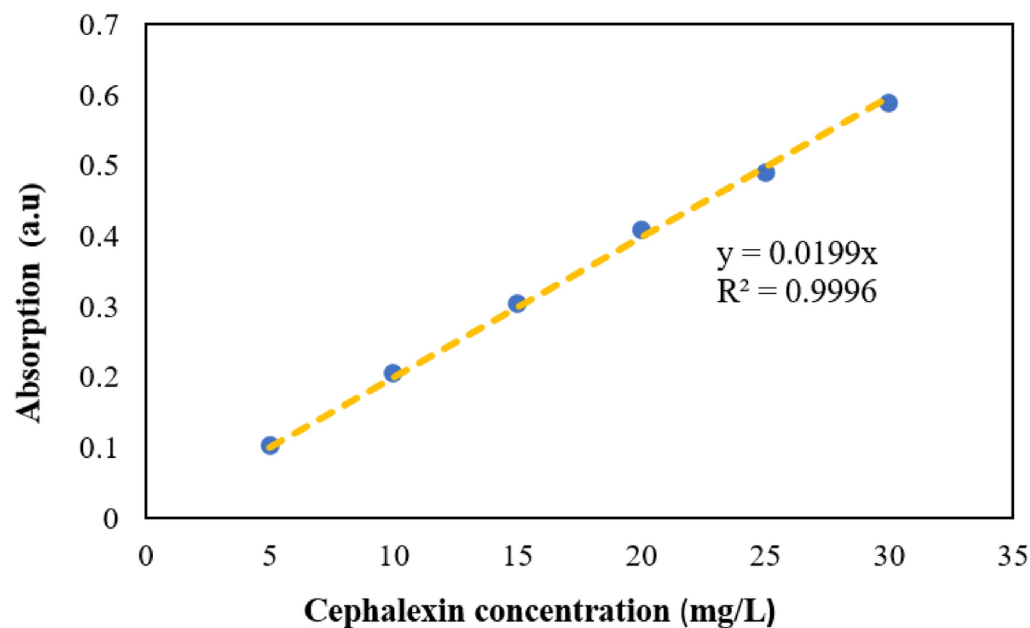


**Fig. 4.** Calibration curve of absorption values versus cephalixin concentration.

Characteristics	Levels		
Level code	−1	0	1
pH	3	6	9
Cephalixin concentration (mg/L)	5	10	15
Catalyst concentration (g/L)	0.5	1	1.5

**Table 5.** Effectiveness levels for photocatalytic degradation of cephalixin using Fe–TiO<sub>2</sub>/Bi<sub>2</sub>O<sub>3</sub> catalysts based on central composite design.

where,  $k$  and  $C_p$  are the number of factors and the replication number of the central point, respectively<sup>77</sup>. In this study, the number of 17 experimental runs was designed according to Eq. (2).

## Results and discussion

### Identifying the optimal Fe–TiO<sub>2</sub>/Bi<sub>2</sub>O<sub>3</sub> nanocatalyst

Three-component Fe–TiO<sub>2</sub>/Bi<sub>2</sub>O<sub>3</sub> catalysts with various weight percentages of Fe<sup>3+</sup>/Ti<sup>4+</sup> and Bi<sub>2</sub>O<sub>3</sub>/TiO<sub>2</sub> have different performance in photocatalytic degradation of aqueous solution of cephalexin. In this regard, to identify the three-component Fe–TiO<sub>2</sub>/Bi<sub>2</sub>O<sub>3</sub> catalyst with highest degradation efficiency of cephalexin, a set of three-component Fe–TiO<sub>2</sub>/Bi<sub>2</sub>O<sub>3</sub> catalysts with different weight percentages of Fe<sup>3+</sup>/Ti<sup>4+</sup> and Bi<sub>2</sub>O<sub>3</sub>/TiO<sub>2</sub> were synthesized, as shown in Table 4. Each catalyst's performance was evaluated using a reactor loaded with 100 mL of cephalexin solution (10 mg/L) under fixed operating conditions (pH 4–5, catalyst dosage of 1 g/L, and a temperature of 25 ± 1 °C) during 240 min of visible light irradiation. According to Fig. 5, upon increasing the Bi<sub>2</sub>O<sub>3</sub>/TiO<sub>2</sub> ratio and reducing Fe<sup>3+</sup>/Ti<sup>4+</sup> in the three-component catalyst increases the degradation efficiency of cephalexin, with the highest degradation efficiency of 54.2%. The optimal three-component catalyst was selected with Fe<sup>3+</sup>/Ti<sup>4+</sup> ratios of 3% and Bi<sub>2</sub>O<sub>3</sub>/TiO<sub>2</sub> ratios of 11% by weight.

### Structural characteristics of nanocatalyst

#### XRD analysis

The crystalline structure and phase composition of as-prepared Fe–TiO<sub>2</sub>/Bi<sub>2</sub>O<sub>3</sub> composite sample were investigated by XRD measurement as shown in Fig. 6. For comparison, pure TiO<sub>2</sub> and Fe–TiO<sub>2</sub> are also included. The XRD pattern of as-prepared TiO<sub>2</sub> shows nine characteristic peaks, at  $2\theta = 25.3^\circ, 37.8^\circ, 48^\circ, 53.8^\circ, 55^\circ, 62.7^\circ, 68.7^\circ, 70.3^\circ$ , and  $75.1^\circ$ , which demonstrates the presence of well-crystallized pure anatase TiO<sub>2</sub> (JCPDS. 21-1272 card No.) and no peaks of rutile and brookite phases were observed in it<sup>2</sup>. Fe-doped TiO<sub>2</sub> diffraction peaks are similar to pure TiO<sub>2</sub><sup>22</sup>. This indicates the presence of a complete anatase phase without the crystalline phase containing iron or iron oxide<sup>55</sup>. This issue could be due to two reasons: (1) the low amount of doped iron ion, and (2) the low calcination temperature applied in the preparation of the nanocatalyst that prevents the reaction of Fe<sup>3+</sup> cations with TiO<sub>2</sub> to form new crystalline phases such as Fe<sub>2</sub>TiO<sub>5</sub> and  $\alpha$ -Fe<sub>2</sub>O<sub>3</sub>. These metal oxides can block TiO<sub>2</sub>'s surface-active sites, reducing the number of active hydroxyl radicals, and consequently decreasing photocatalytic activity. It can be concluded that since the ion radii of Ti<sup>4+</sup> and Fe<sup>3+</sup> are 0.068 and 0.064 nm, respectively, and are almost the same, it can be inferred that Fe ions might insert into the structure of titanium and locate at interstices or occupy some of the lattice sites of TiO<sub>2</sub>, and thus iron ion doping is performed with titanium<sup>78,79</sup>. Only the diffraction peaks of anatase phase TiO<sub>2</sub> were observed in the XRD map of the Fe–Bi<sub>2</sub>O<sub>3</sub>/TiO<sub>2</sub> composite catalyst, there was no detection of Bi<sub>2</sub>O<sub>3</sub> diffraction peaks, which indicates that Bi<sub>2</sub>O<sub>3</sub> did not form a separate crystallization phase. The reason can be either the extremely high dispersion of the Bi<sub>2</sub>O<sub>3</sub> particles in the anatase phase TiO<sub>2</sub> crystal, or the low Bi<sub>2</sub>O<sub>3</sub> content<sup>80,81</sup>. Since the crystallinity of titania samples is crucial important for photocatalytic efficiency, the size of the particles was calculated using Scherer's equation (Eq. 3) for the three peaks with greater intensity for the catalysts<sup>82</sup>

$$d = \frac{k\lambda}{\beta \cos \theta} \quad (3)$$

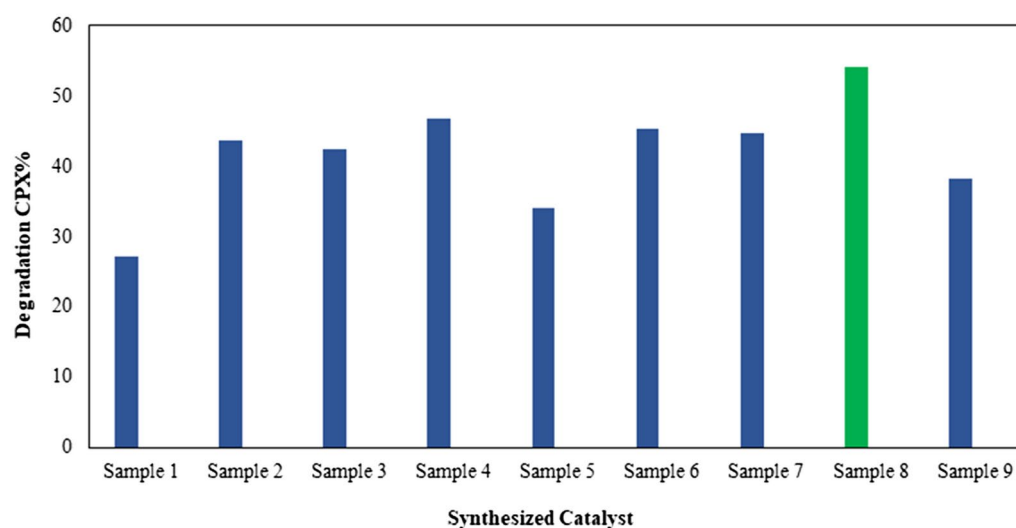


**Fig. 5.** Cephalexin degradation efficiency using Fe–TiO<sub>2</sub>/Bi<sub>2</sub>O<sub>3</sub> three-component catalysts (Table 4) under a unique operating condition (solution pH of 4.5, a cephalexin concentration of 10 mg/L, and a catalyst concentration of 1 g/L during 240 min of visible light irradiation).



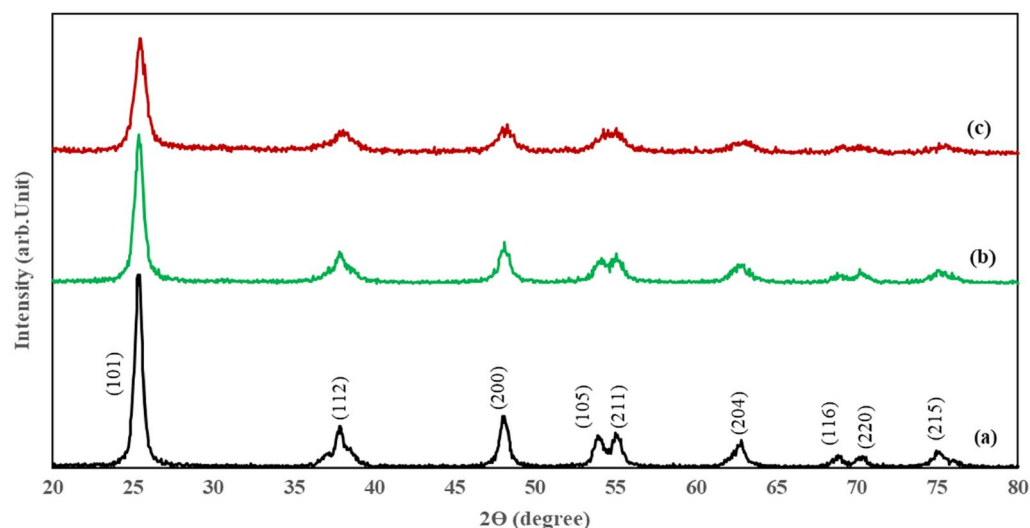


**Fig. 6.** XRD pattern of samples (a)  $\text{TiO}_2$ , (b)  $\text{Fe-TiO}_2$  with  $\text{Fe}^{3+}/\text{Ti}^{4+} = 3\%$  (wt. ratio) and (c)  $\text{Fe-TiO}_2/\text{Bi}_2\text{O}_3$  with optimal weight ratios of  $\text{Fe}^{3+}/\text{Ti}^{4+}$  and  $\text{Bi}_2\text{O}_3/\text{TiO}_2$  components, respectively 3 and 11 percent.

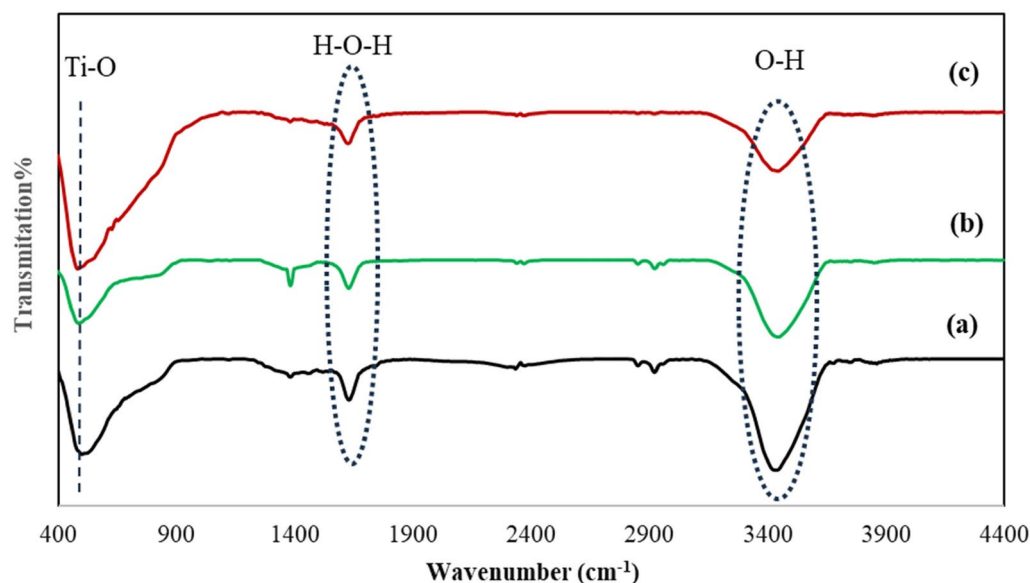


**Fig. 7.** FT-IR analysis of samples (a)  $\text{TiO}_2$ , (b)  $\text{Fe-TiO}_2$  with  $\text{Fe}^{3+}/\text{Ti}^{4+} = 3\%$  (wt. ratio) and (c)  $\text{Fe-TiO}_2/\text{Bi}_2\text{O}_3$  with optimal weight ratios of  $\text{Fe}^{3+}/\text{Ti}^{4+}$  and  $\text{Bi}_2\text{O}_3/\text{TiO}_2$  components, respectively 3 and 11 percent.

where  $d$  is the average crystal size,  $\lambda$  is X-ray wavelength,  $k$  is the shape factor (constant),  $\beta$  is full width at maximum half intensity (FWHM), and  $\theta$  is half-angle diffraction. The average crystal size for pure  $\text{TiO}_2$ ,  $\text{Fe-TiO}_2$  and  $\text{Fe-TiO}_2/\text{Bi}_2\text{O}_3$  three-component catalyst were calculated as 15.6, 13.9 and 10.2 nm, respectively. The values show that  $\text{Fe-TiO}_2$  and  $\text{Fe-TiO}_2/\text{Bi}_2\text{O}_3$  have smaller crystal sizes than pure  $\text{TiO}_2$ . As shown in Fig. 6, the intensity of anatase  $\text{TiO}_2$  peaks decreases with the addition of Fe and  $\text{Bi}_2\text{O}_3$ , owing to anatase's decreased crystalline size. This is due to the presence of Fe, which prevents nanocrystal growth by inhibiting the extension of Ti-O-Ti bridging, or causes defective crystallographic point formation by replacing  $\text{Ti}^{4+}$  cations with  $\text{Fe}^{3+}$  ions<sup>83</sup>.

#### FT-IR analysis

Fourier transform-infrared spectra is based on the absorption of radiation and investigation of vibrational transitions of molecules and polyatomic ions, which is used to determine the structure and measurement of chemical species. The molecular geometry and interactions of the functional groups existing in the system of the synthesized catalysts were determined by FTIR spectra. FTIR spectra of pure  $\text{TiO}_2$ ,  $\text{Fe-TiO}_2$  and optimal  $\text{Fe-TiO}_2/\text{Bi}_2\text{O}_3$  photocatalysts in the wavenumber range 400–4000  $\text{cm}^{-1}$  can be observed in Fig. 7. The position and

intensity of IR peaks are strongly influenced by the crystallization behavior, morphology, and particle size. The band at  $3450\text{ cm}^{-1}$  is ascribed to the stretching mode of OH group on the catalyst<sup>84</sup>, corresponds to the presence of water molecules and also a low-intensity signal at  $1628\text{ cm}^{-1}$  due to the bending vibrations of adsorbed  $\text{H}_2\text{O}$  on catalyst surface. Photocatalytic activity increases in the presence of hydroxyl groups because the OH groups serve as the main scavenger of the photogenerated charge carrier, which leads to the formation of a hydroxyl radical ( $\text{OH}\cdot$ ) with the high redox potential (2.8V), and played effective role in degradation of pollutant<sup>72,85</sup>. The absorption band of  $520\text{ cm}^{-1}$  is related to the bonding of the Ti–O–Ti group<sup>84</sup>. According to previous research, in Fe– $\text{TiO}_2$  powders any band corresponding to iron phases were not observed<sup>79,84</sup>. The absorption band at  $740\text{ cm}^{-1}$  is related to the stretching vibration of Bi–O, which, according to Fig. 7, has a negligible intensity. In the FTIR spectrum of the three-component composite compared to  $\text{TiO}_2$  and Fe-doped  $\text{TiO}_2$ , no significant difference was observed and only the displacement of the Ti–O–Ti group and the decrease in the absorption intensity of the OH band occurred. This can be due to the combination of materials and the confirmation of the formation of the composite material<sup>86</sup>.

#### DRS analysis

The photocatalytic performance of a semiconductor is highly dependent on the structure of electron layers and its energy gap. Since the light absorption edge in semiconductors is related to the energy gap, it seems necessary to investigate the optical properties of catalysts. Therefore, the optical properties and band gap energy of the synthesized catalysts were investigated with the help of a UV–Vis emission-penetration spectrometer in the wavelength range of 300 to 600 nm. The indirect bandgap of pure  $\text{TiO}_2$  and Fe-doped  $\text{TiO}_2$  and Fe– $\text{TiO}_2/\text{Bi}_2\text{O}_3$  nanoparticles was determined from the linearity of a plot of  $(F(R)h\nu)^{1/2}$  versus photon energy ( $h\nu$ ) respectively. The absorption spectra are acquired from reflectance using Kubelka–Munk function  $h\nu = 1240/\lambda$  and  $F(R) = (1 - R)^2/(2R)$ , where R is the reflectance of the sample<sup>79,85,87</sup>. Figure 8 shows the plots of  $(F(R)h\nu)^{1/2}$  versus ( $h\nu$ ). According to Fig. 8, the energy band gap values of the samples are 3.27, 2.91 and 2.82 eV for  $\text{TiO}_2$ , Fe doped  $\text{TiO}_2$  and Fe– $\text{TiO}_2/\text{Bi}_2\text{O}_3$  nano-composite, respectively. The doping of Fe and addition bismuth oxide to titanium dioxide has reduced the energy band gap in the composite.  $\text{Fe}^{3+}$  ions can creates new  $e^-/h^+$  and traps energy levels ( $\text{Fe}^{4+}/\text{Fe}^{3+}$  and  $\text{Fe}^{3+}/\text{Fe}^{2+}$ ) between the conduction band and valence band of  $\text{TiO}_2$  precursors<sup>88</sup> or it can enters into the  $\text{TiO}_2$  lattice and uniformly replaces part of  $\text{Ti}^{4+}$ , resulting in enhanced visible absorption and the narrow band gap<sup>87</sup>. Although the addition of bismuth oxide showed minor shift in absorption edge towards higher wavelength, the photocatalytic activity of the Fe– $\text{TiO}_2/\text{Bi}_2\text{O}_3$  composite has increased under visible light irradiation. This may be due to multiple reflections of light with mixed nanostructures which increases the incident time to utilize more photons<sup>89</sup>.

#### FE-SEM, EDX analysis

The FE-SEM image and the EDX results of synthesized catalysts are illustrated in Fig. 9 exhibited an agglomerated structure with an irregular surface. Agglomeration may be caused by small nanoparticles with a higher surface area or insufficient dispersion of nanoparticles during the synthesis process<sup>82</sup>. The Fig. 9 show that Fe-doped  $\text{TiO}_2$  powder consist of nanosized primary particles agglomerated together, whereas pure  $\text{TiO}_2$  powder rconsists of relatively larger chunks of powdered particles that are micron in size<sup>90</sup>. By examining Fig. 9b, it can be seen that the growth of particles is controlled by  $\text{Fe}^{3+}$  doping, which is very important for the design of surface

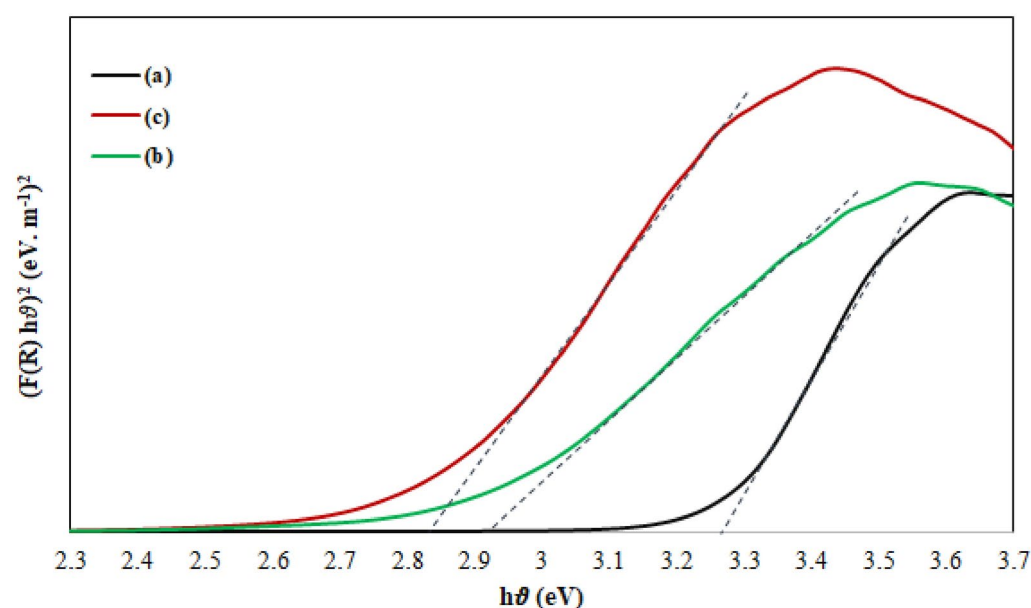


**Fig. 8.** Band gap energy for samples (a)  $\text{TiO}_2$ , (b) Fe– $\text{TiO}_2$  with a weight ratio of 3%  $\text{Fe}^{3+}/\text{Ti}^{4+}$  and (c) optimal ternary composite.

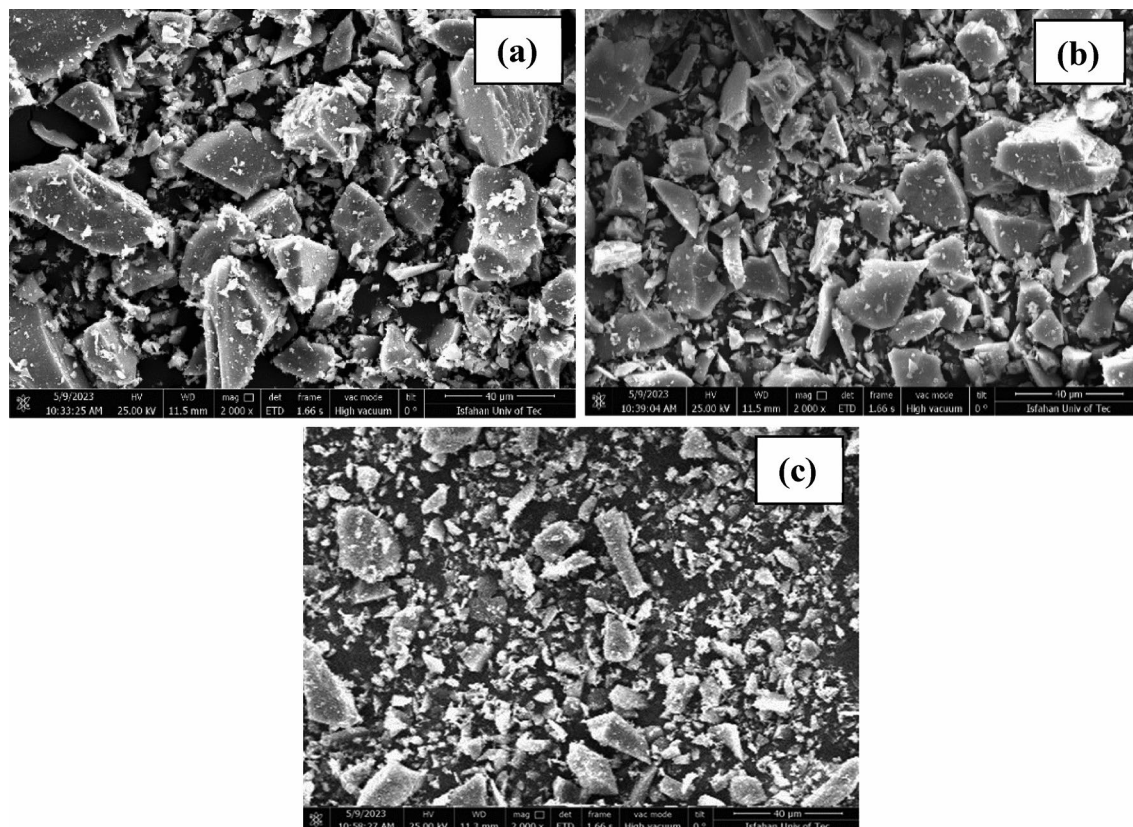


**Fig. 9.** FE-SEM analysis of samples (a)  $\text{TiO}_2$ , (b)  $\text{Fe-TiO}_2$  with a weight ratio of  $\text{Fe}^{3+}/\text{Ti}^{4+} = 3\%$  and (c) optimal three-component composite.

features. The morphology obtained for Fe-doped  $\text{TiO}_2$  is consistent with previous studies<sup>82,91,92</sup>. According to Fig. 9c, the optimal three-component  $\text{Fe-TiO}_2/\text{Bi}_2\text{O}_3$  composite compared to the two-component  $\text{Fe-TiO}_2$  catalyst with a weight ratio of  $\text{Fe}^{3+}/\text{Ti}^{4+} = 3\%$  is composed of smaller polyhedral particles with straight edges and sharp corners. The EDX results (Fig. 10) confirm the presence of all of the elements in catalysts and prove the catalysts has been successfully synthesized without any additional elements.

### Evaluation of operational parameters and process optimization by RSM

In this research, the effect of three variables were investigated in the photocatalytic degradation of cephalexin with  $\text{Fe-TiO}_2/\text{Bi}_2\text{O}_3$  powder nanocatalyst under visible light irradiation. Box-Behnken design for RSM was used for the experimental design. The obtained actual results are presented in Table 6. The central point of the initial cephalexin concentration, the nanocatalyst concentration and pH in the experiments are 10 mg/L, 1g/L and 6, respectively. Under this operating conditions, 3 tests were repeated, which is for statical evaluation of the experiment's accuracy. To fit the data and specify an appropriate mathematical model to express the relationship between the involved operational variables in form of quadratic, polynomial Eq. (4).

$$Y(\%) = b_0 + b_1X_1 + b_2X_2 + b_3X_3 + b_{12}X_1X_2 + b_{13}X_1X_3 + b_{23}X_2X_3 + b_{11}X_1^2 + b_{22}X_2^2 + b_{33}X_3^2 \quad (4)$$

In this relationship, Y is the dependent variable, X is the independent variable, and  $b_i$ ,  $b_{ii}$ , and  $b_{ij}$  are linear and quadratic fitting coefficients,  $b_{ii}$  is the influence coefficient of the second term of variable i, and  $b_{ij}$  is the simultaneous influence coefficient of variables i and j.

Initially statistical analysis of the data obtained from the cephalexin degradation tests was performed using the analysis of variance method. The results of the analysis for the optimal three-component catalyst are presented in Table 7. The initial pH of the pollutant solution, the concentration of the catalyst (g/L) and the initial concentration of the cephalexin pollutant (mg/L) are respectively coded as A-pH, B-Cat and C-CPX, respectively. Factors whose *p*-value is less than 0.05 are considered effective factors. In addition, the *p*-value (<0.0001) shows the high importance of the model sentences. Also, terms with *p*-value (>0.1) are insignificant in the model. As can be seen in Table 7, the AC, BC,  $A^2$ , and  $C^2$  terms with P values of 0.8804, 0.6406, 0.5849, and 0.6910, respectively are less important than other terms, and the fit accuracy is improved by their removal.

In some cases, it is important to make changes in response power ( $y^* = y^\lambda$ ); that  $\lambda$  should be determined as the conversion characteristic. Box-Cox diagram suggests an appropriate power transfer function for this data. By choosing the power function and setting its power equal to 0.27 according to Fig. 11, a proper analysis of the data was obtained that, are presented in Table 8. By comparison of paparameters in two tables of 7 and 8 appropriateness

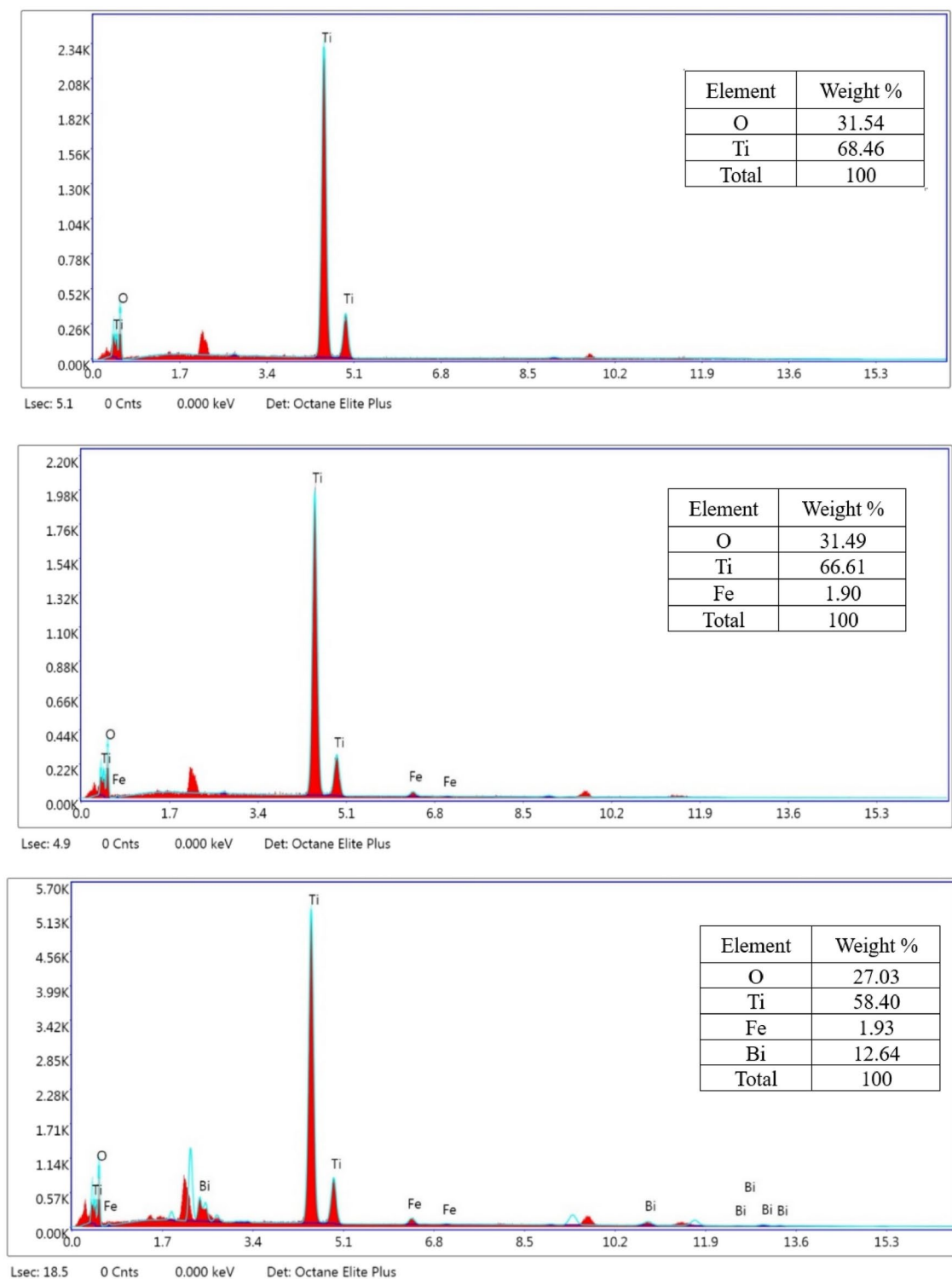


**Fig. 10.** EDX analysis of samples (a) TiO<sub>2</sub>, (b) Fe–TiO<sub>2</sub> with a weight ratio of Fe<sup>3+</sup>/Ti<sup>4+</sup> = 3% and (c) optimal three-component composite.

can be identified, e.g., F-value of lack-of-fit parameter that predicts the deviation of the data around the fitted model. The *p*-value of this parameter should be above 0.05, otherwise, the error of the presented model become important. According to Table 8, the F-value of lack-of-fit is 5.85, while its *p*-value is equal to 0.1544, which confirms the model error is not important, i.e., the deviation of the data around the fitted model is acceptable.

Statistical model for the degradation efficiency of cephalexin for the optimal catalyst is presented by Eq. (5) where pH is initial pH of the solution, [Cat] and [CPX] are catalyst concentration (g/L) and cephalexin concentration (ppm), respectively.

Test	Initial pH	Catalyst concentration (g/L)	Cephalexin concentration (mg/L)	Cephalexin degradation efficiency (%)
1	9	1.5	5	73.4
2	6	1	15	48.97
3	6	0.5	10	46
4	9	1	10	61.07
5	3	1	10	49.02
6	3	0.5	15	35.51
7	6	1	5	60.7
8	3	1.5	5	54.08
9	9	0.5	5	51.42
10	3	0.5	5	42
11	9	1.5	15	65.89
12	3	1.5	15	47.23
13	9	0.5	15	46.55
14	6	1	10	52.6
15	6	1	10	51.48
16	6	1	10	53
17	6	1.5	10	57.46

**Table 6.** Operational parameters range in the designed experiments and actual results in terms of cephalexin removal.

Source	Sum of squares	df	Mean square	F-value	p-value	Suggestion
Model	1281.28	9	142.36	30.11	<0.0001	Significant
A-pH	496.88	1	496.88	105.11	<0.0001	Significant
B-Cat	586.45	1	586.45	124.05	<0.0001	Significant
C-CPX	140.25	1	140.25	29.67	0.0010	Significant
AB	38.37	1	38.37	8.12	0.0247	Significant
AC	0.1152	1	0.1152	0.0244	0.8804	Not Significant
BC	1.13	1	1.13	0.2380	0.6406	Not Significant
A <sup>2</sup>	1.55	1	1.55	0.3278	0.5849	Not Significant
B <sup>2</sup>	17.48	1	17.48	3.70	0.0959	Significant
C <sup>2</sup>	0.8119	1	0.8119	0.1717	0.6910	Not Significant
Residual	33.09	7	4.73			
Lack of fit	31.85	5	6.37	10.26	0.0912	Not significant
Pure error	1.24	2	0.6208			
Cor total	1314.37	16				

**Table 7.** ANOVA results for the quadratic model.

$$\begin{aligned}
 (\text{Degradation of CPX})^{0.27} &= 2.538 + 0.021 * \text{pH} + 0.448 * [\text{Cat}] \\
 &- 0.011 * [\text{CPX}] + 0.014 * \text{pH} * [\text{Cat}] - 0.151 * [\text{Cat}]^2 \quad R^2 = 0.97
 \end{aligned}
 \tag{5}$$

According to Table 9, the predicted and adjusted  $R^2$  are 0.9428 and 0.9615, respectively. The  $R^2$  parameters determines the accuracy of a model for predicting the results and matching the laboratory answers with the predicted ones by the model. As difference of  $R^2$  (predicted and adjusted  $R^2$ ) values is less than 0.2 the model is proper and acceptable. The closer this parameter is to one, the more accurate the model is. The Adeq Precision compares the range of predicted values at design points with the predicted error average, and this value measures the signal-to-noise ratio. A ratio greater than 4 is desirable<sup>95</sup>. In this study, the characteristic value of adequate precision equal to 35.1513 that indicates the predicted model is appropriate. According to the F values of operational variables as presented in Table 8, concentration of the catalyst and pH of the solution are the most effective parameters in the degradation of cephalexin. Figure 12 depicts a linear relationship between experimental data and predicted values for cephalexin removal. It confirms the proposed model's accuracy because all of the data converged on a 45-degree line. Figure 12b depicts the normal probability plot of the residuals, which clearly shows linear scattering of the modeling data. The linear scattering means normal distribution of errors in a defined matrix for experimental design. Therefore, the probability of random error intervention and effect of the sequence of experiments is considerably decreased in the proposed model.



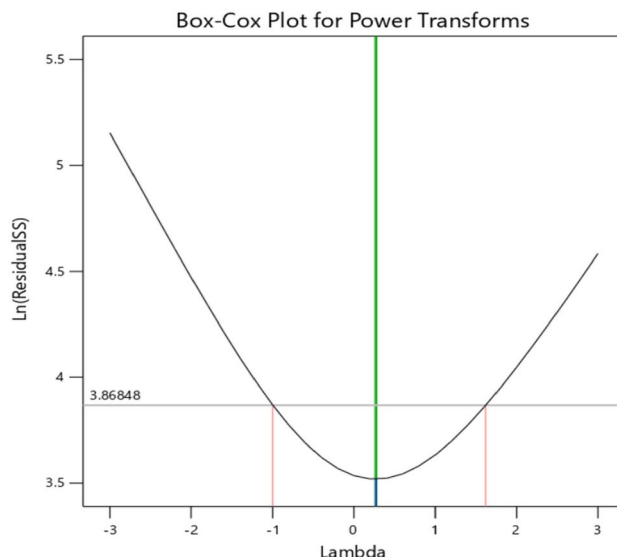


**Fig. 11.** Box–Cox plot of output responses based on the RSM.

Source	Sum of squares	df	Mean square	F-value	p-value	Suggestion
Model	0.2825	5	0.0565	80.87	<0.0001	Significant
A-pH	0.1095	1	0.1095	156.76	<0.0001	Significant
B-Cat	0.1316	1	0.1316	188.40	<0.0001	Significant
C-CPX	0.0320	1	0.0320	45.87	<0.0001	Significant
AB	0.0034	1	0.0034	4.93	0.0483	Significant
B <sup>2</sup>	0.0059	1	0.0059	8.38	0.0146	Significant
Residual	0.0077	11	0.0007			
Lack of Fit	0.0074	9	0.0008	5.85	0.1544	Not significant
Pure Error	0.0003	2	0.0001			
Cor Total	0.2902	16				

**Table 8.** Modified ANOVA results for the quadratic model.

Property	Value	Property	Value
Std. Dev <sup>a</sup>	0.0264	R <sup>2</sup>	0.9735
Mean	2.91	Adjusted R <sup>2</sup>	0.9615
C.V <sup>b</sup> %	0.9086	Predicted R <sup>2</sup>	0.9428
		Adequate Precision	35.1513

**Table 9.** Statistical summary of the selected model for the efficiency of photocatalytic degradation of cephalixin with optimal three-component composite. <sup>a</sup>Standard deviation. <sup>b</sup>Coefficient of variation.

Figure 13 illustrates the individual effects of operational parameters on cephalixin removal. In this study, contour lines mean the performance of the optimal photocatalyst for cephalixin removal at different operating parameters. The contour map reflects the cross-interaction between two variables by keeping the other variable constant. At low concentrations, the pollutant can easily reach the catalyst's active surface and react with the produced free radicals. However, as pollutant concentration increases, the number of active sites accessible to the light beam and the pollutant decreases, that results in decreasing of degradation efficiency. The upward trend in pollutant degradation efficiency with increasing catalyst concentration can be attributed to an increase in the number of available active sites and absorbed photons, which leads to more hydroxyl radical production and consequently improving photocatalytic degradation. Furthermore, by increasing the pH of the solution (above 10), the competition of pollutant molecules with hydroxyl radicals for absorption by the catalyst and also the production of radicals with lower activity compared to hydroxyl radicals, reduces the efficiency of photocatalytic degradation.



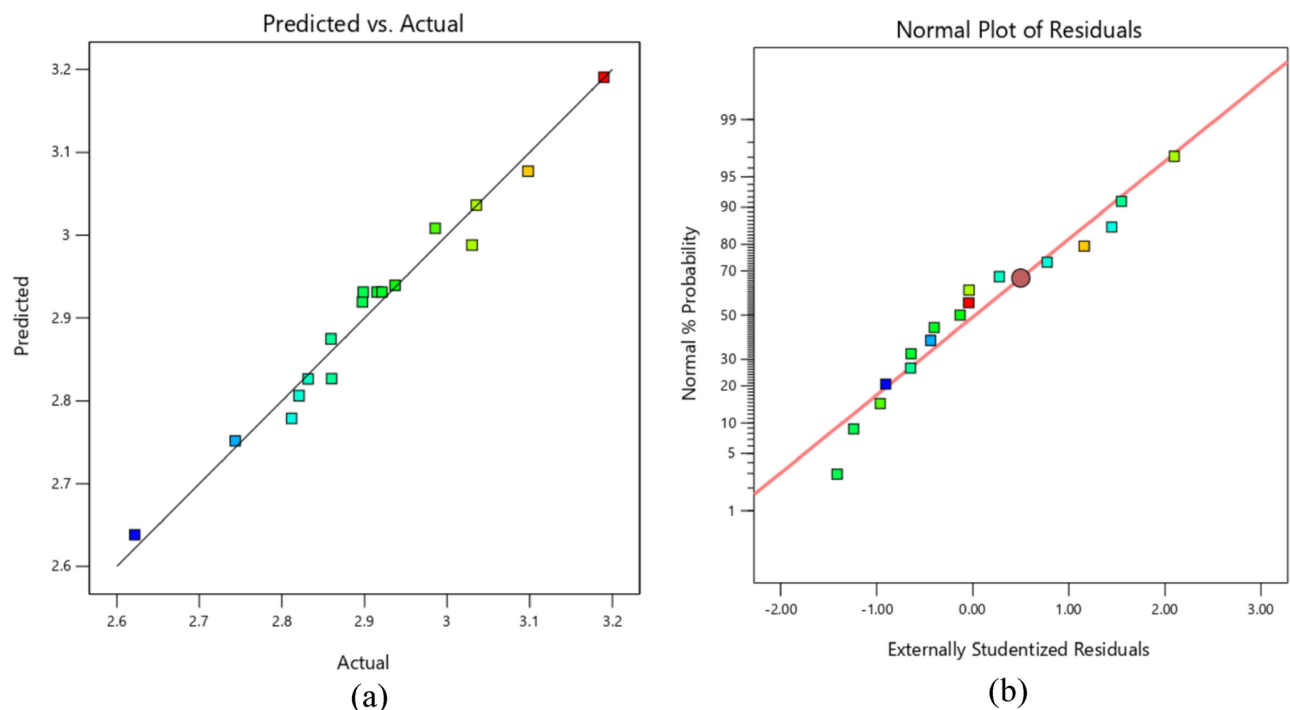


**Fig. 12.** Presentation (a) relationship of predicted and corresponding actual values of the statistical model for cephalixin removal; (b) the externally studentized residuals versus normal % probability distribution.

An optimization was performed to find the optimal operating conditions for the removal of cephalixin from the synthetic solutions. The optimal conditions for the characteristics of solution pH, cephalixin concentration, and photocatalyst concentration were determined by the derived model are 9, 5 mg/L, and 1.5 g/L, respectively. In this case, the highest efficiency of cephalixin degradation was predicted by the software to be 73.5%. By performing an experiment under the mentioned optimal conditions, the removal efficiency of cephalixin was 73.4%. The agreement between the predicted and experimental results, also confirms the validity of the derived model. Photocatalytic degradation of cephalixin by using the optimal three-component catalyst under optimal operating conditions was also investigated by application of ultraviolet light, with a power source of 15 W for a period of 240 min. Photocatalytic activity of cephalixin degradation under the mentioned conditions was experimentally measured as 96% at 120 min.

### Reusability Fe doped $\text{TiO}_2/\text{Bi}_2\text{O}_3$ photocatalyst

Reusability of the Fe (3 wt%) doped  $\text{TiO}_2\text{-Bi}_2\text{O}_3$  (11 wt%) photocatalyst for degradation of Cephalixin was studied at optimum conditions. Figure 14 displays Cephalixin removal efficiency and recovered photocatalyst (wt.%) for 5 cycles. After the first cycle, the catalyst was recovered by centrifugation, washed with distilled water then dried at 80 °C for 2 h. The result showed that the photocatalytic activity reduces about 4% after 5 cycles. It is confirmed that the reused catalyst has a stable structure and could be used in the subsequent runs with relatively sustainable catalytic activity.

### Kinetic study

Kinetic study was done to calculate the rate constant of cephalixin photodegradation for Fe- $\text{TiO}_2\text{-Bi}_2\text{O}_3$  at different concentrations. The pseudo-first-order kinetic model was used to study the photodegradation kinetic for most of the organic molecules as described<sup>11,94</sup>:

$$\ln \left( \frac{C_0}{C_t} \right) = k * t \quad (6)$$

where  $C_0$  (mg/L), the initial concentration of cephalixin,  $C$  (mg/L), the concentration at time (t) after irradiation, and  $k$  is a pseudo-first-order rate constant. The kinetic plot ( $\ln(C_0/C_t)$  versus irradiation time) was depicted in Fig. 15, the pseudo-first-order rate constant was determined based on a straight-line slope. According to the results of Fig. 15, the maximum reaction rate at the initial concentration of 5 mg/L cephalixin is  $0.0062 \text{ min}^{-1}$ , which is about 2 times higher than the obtained reaction rate at the initial concentration of 15 mg/L cephalixin. The results show that reaction rates decrease with increasing concentration.

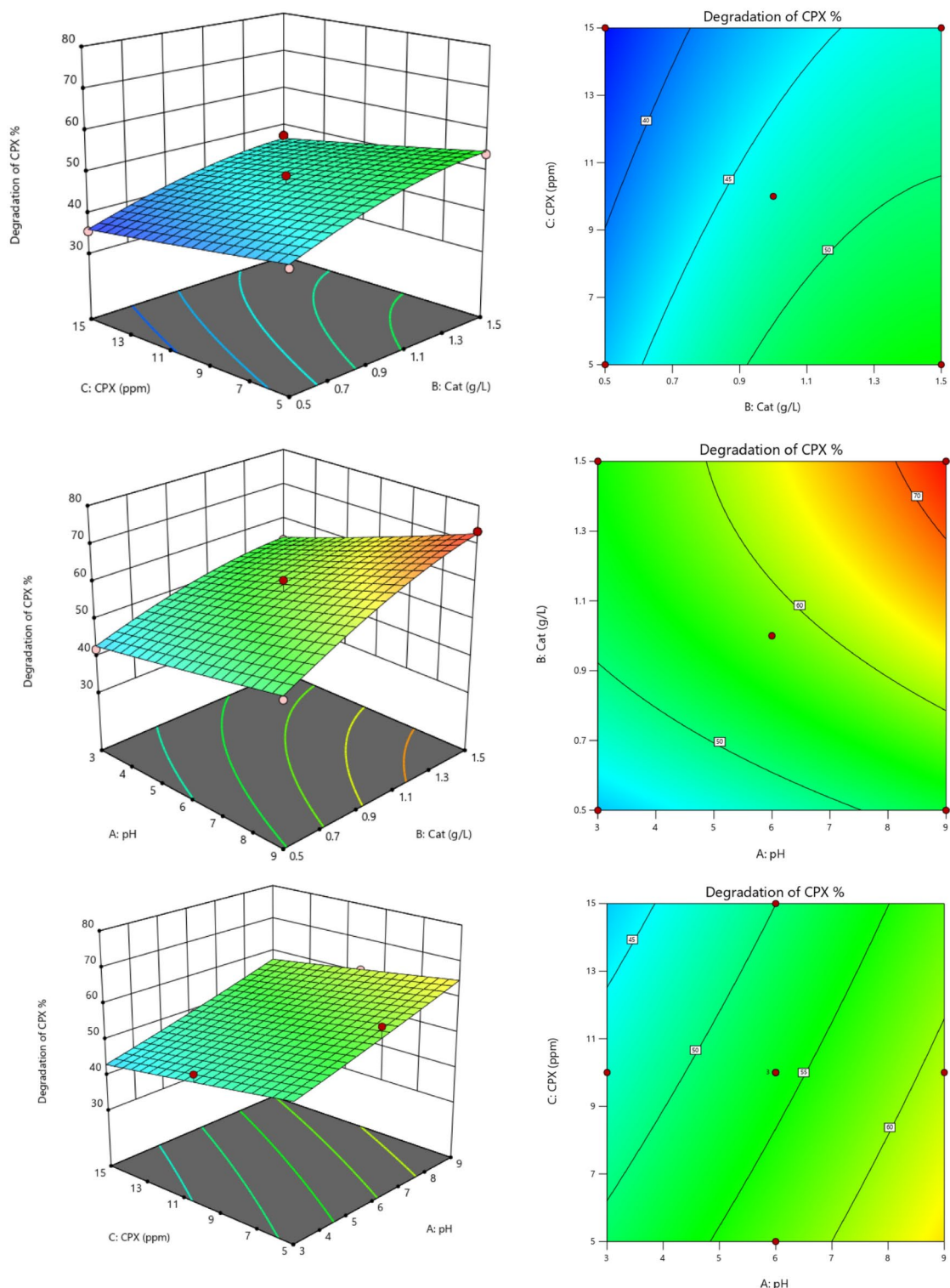


**Fig. 13.** Presentation of the effect of operating characteristics on degradation of cephalixin efficiency for the optimal three-component catalyst (a) catalyst and cephalixin concentration, (b) catalyst concentration and pH, (c) cephalixin concentration and pH.

### Possible photodegradation mechanism

Photogenerated electrons and holes in the valence band (VB) and conduction band (CB) of the photocatalyst interact with water ( $H_2O$ ) and oxygen ( $O_2$ ). The identification of the primary active species is crucial for proposing a photocatalytic mechanism. Therefore, various scavengers were introduced into the reaction solution to conduct radical trapping experiments. In this study, BQ, EDTA,  $AgNO_2$ , and IPA were used as trapping

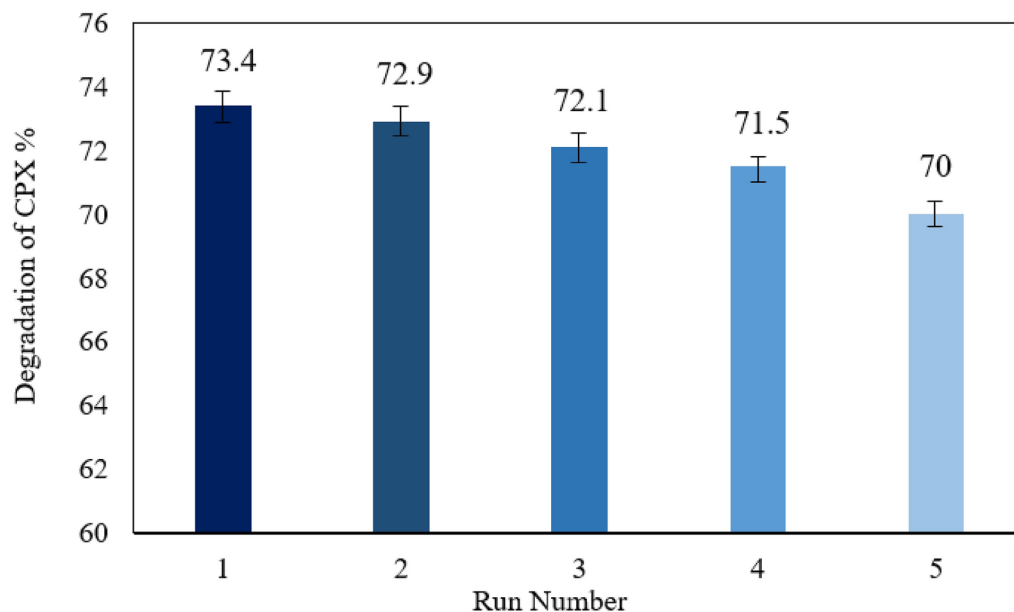


**Fig. 14.** Reusability and regeneration of optimal catalyst for cephalixin degradation.

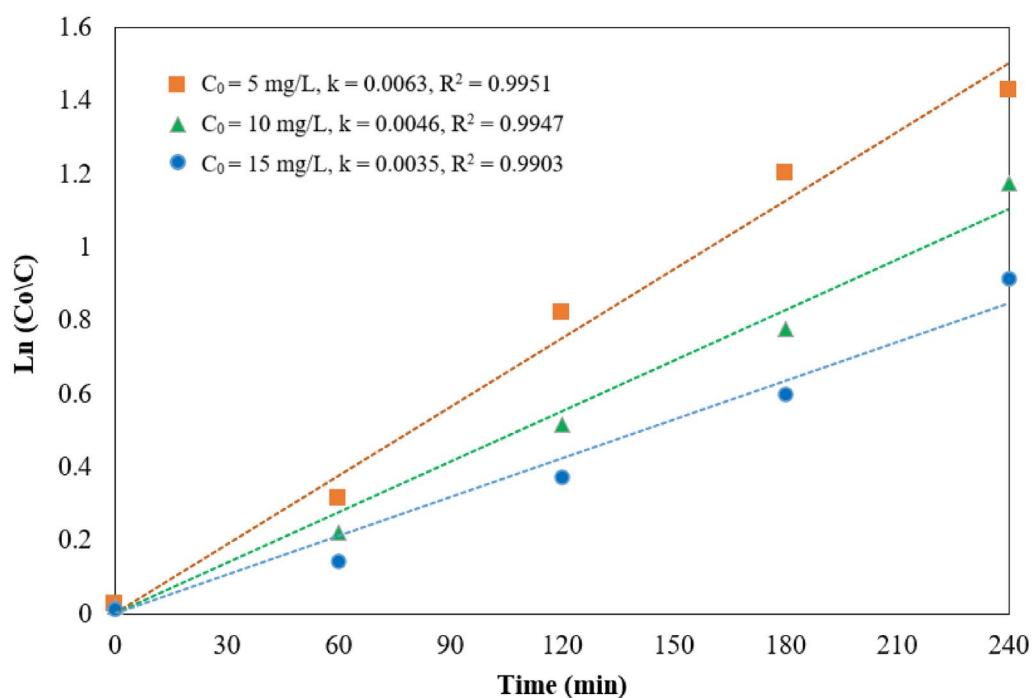


**Fig. 15.** Effect of initial CPX concentration on the photodegradation kinetics under optimal conditions.

agents to investigate the roles of superoxide radicals, holes, electrons, and hydroxyl radicals, respectively, under optimal conditions (Fig. 16). The introduction of IPA significantly reduced photocatalytic efficiency, which shows that hydroxyl radicals are the main active species due to its strong oxidant ability and non-selectivity in the CEX photodegradation process, and the role of other species decreases in this order: superoxide radicals > hole > electron. As shown in Fig. 17, under visible light irradiation, photoinduced electrons and holes are generated, resulting in the formation of active radical species for the decomposition of CPX drugs. The reaction between dissolved oxygen ( $O_2$ ) and photogenerated electrons produces reactive species that contribute to the degradation of CEX molecules. Additionally, photoinduced holes and adsorbed CPX on the photocatalyst interface can directly generate reactive  $CEX^+$  radicals. The obtained CFX removal efficiencies by different photocatalysts are compared with the results of this study and listed in Table 10. In this study, the  $Fe-TiO_2/$

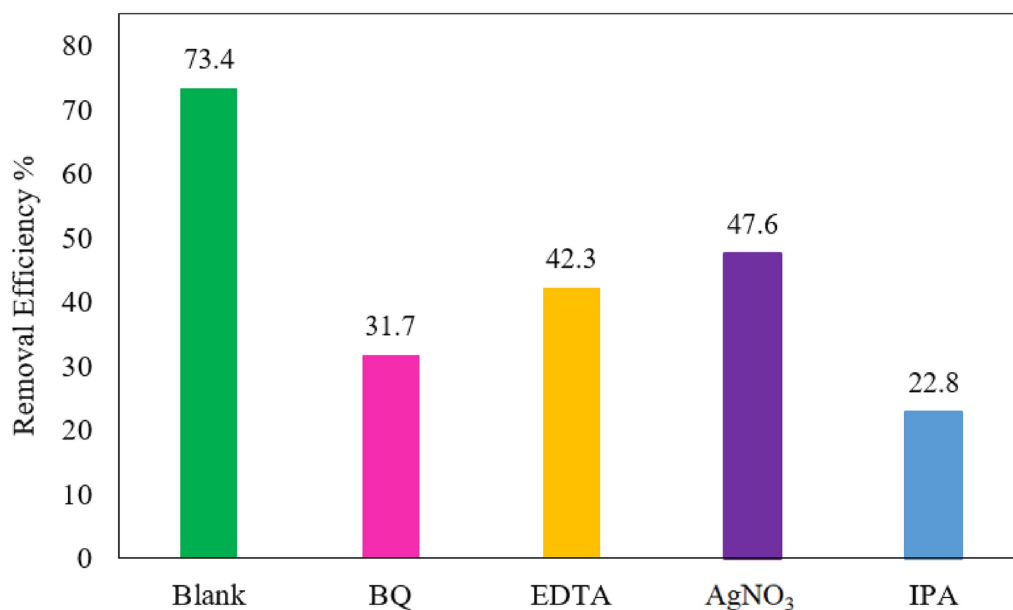


**Fig. 16.** The removal efficiency of CPX by Fe-TiO<sub>2</sub>/Bi<sub>2</sub>O<sub>3</sub> in the presence of trapping agents under optimum conditions (pH=9, catalyst dosage 1.5 g/L, CPX concentration 5 ppm, irradiation time 240 min).

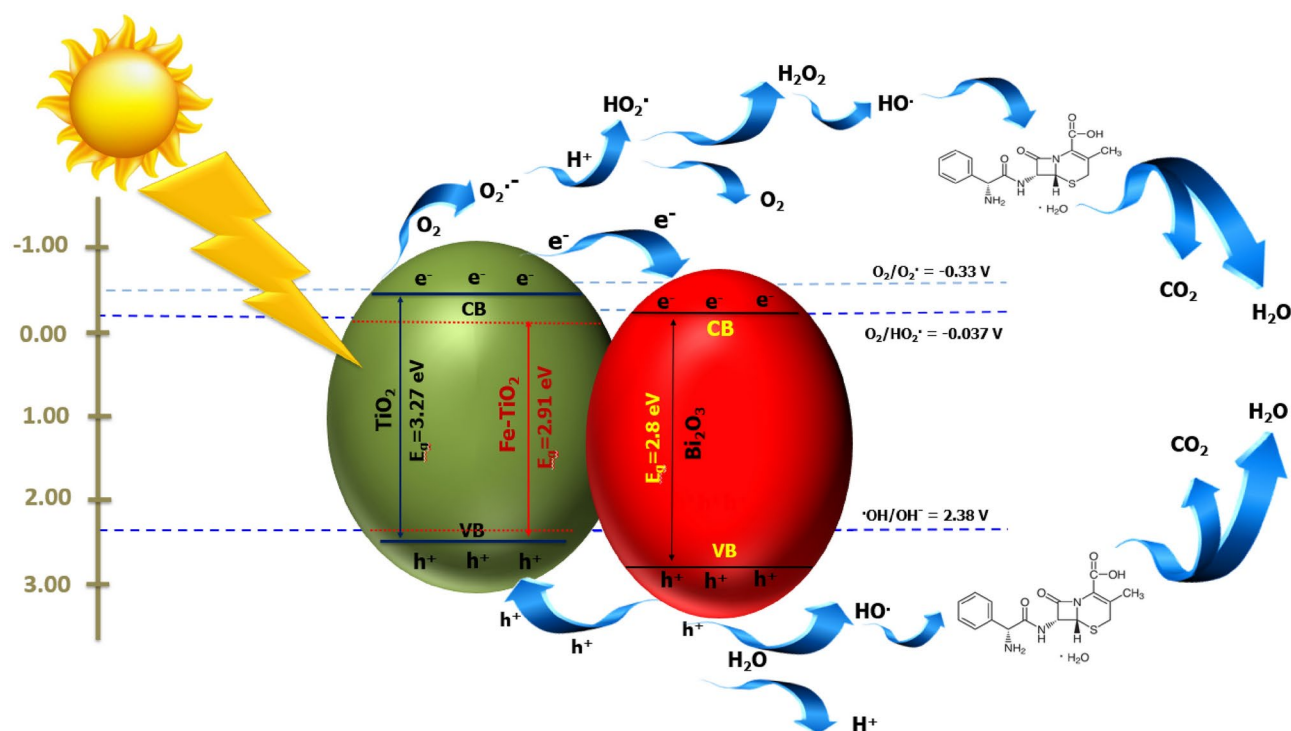


**Fig. 17.** Schematic diagram of photodegradation of CPX under Fe-TiO<sub>2</sub>/Bi<sub>2</sub>O<sub>3</sub>.

Bi<sub>2</sub>O<sub>3</sub> photocatalyst under visible light, achieved about 74% removal efficiency for cephalexin in 240 min and 96% at 120 min under UV irradiation. Although some previous studies have reported faster degradation rates, the longer reaction time observed here is balanced by the significant economic and environmental benefits of using visible light.

Type of photocatalyst	Optimal condition	Illumination	Removal efficiency Irradiation time	References
N-TiO <sub>2</sub> /ZnFe <sub>2</sub> O <sub>4</sub> /zeolite	Catalyst dose: 2 g/L CPX concentration: 100 ppm pH: 7	Two visible LED lamps (200 W)	74%, 120 min	<sup>51</sup>
NiS-PPY-Fe <sub>3</sub> O <sub>4</sub>	Catalyst dose: 0.2 g/L pH: 7	Hg-Lump (75W)	85%, 360 min	<sup>95</sup>
NiO-clinoptilolite	Catalyst dose: 0.2 g/L pH: 4.5	medium pressure Hg lamp (75 W)	76%, 300 min	<sup>96</sup>
Clinoptilolite-supported hybridized PbS-CdS	Catalyst dose: 1.5 g/L CPX concentration: 100 folds diluted solution pH: 3	Two UV tubes each of (35 W)	52%, 500 min	<sup>97</sup>
TiO <sub>2</sub>	Catalyst dose: 2 g/L CPX concentration: 5 ppm pH: 7	UV (18W)	63.5%, 45 min	<sup>98</sup>
Bi <sub>2</sub> WO <sub>6</sub> /CNT/TiO <sub>2</sub>	Catalyst dose: 0.75 g/L CPX concentration: 20 ppm pH: 5	Xenon lamp (300W)	89.7%, 70 min	<sup>2</sup>
CuWO <sub>4</sub> /Bi <sub>2</sub> S <sub>3</sub>	Catalyst dose: 0.8 g/L CPX concentration: 10 ppm pH: 3	Blue light LED	81.7% ,150 min	<sup>27</sup>
Fe-TiO <sub>2</sub> /Bi <sub>2</sub> O <sub>3</sub>	Catalyst dose: 1.5 CPX concentration: 5 ppm pH: 9	Visible (50W) UVA (15W)	73.4%,240 min 96%.120 min	This Study

**Table 10.** Comparison of previous reports with the current study results for CPX photodegradation.

## Conclusion

In summary, we synthesized a novel Fe-doped TiO<sub>2</sub>/Bi<sub>2</sub>O<sub>3</sub> ternary composite system using a sol-gel method for the degradation of the antibiotic cephalexin. The effect of operating parameters, including initial cephalexin concentration, initial pH, and photocatalyst dosage on the degradation of cephalexin was investigated. The DRS test results demonstrated that modifying the titanium dioxide nanocatalyst with iron metal and bismuth oxide semiconductor shifted the absorption wavelength from the ultraviolet region to the visible region. The position of XRD diffraction peaks in modified samples was the same as in pure TiO<sub>2</sub>. However, the intensity of the anatase peaks in TiO<sub>2</sub> was reduced due to the addition of Fe and Bi<sub>2</sub>O<sub>3</sub>, which caused a decrease in the size of the anatase crystals. Optimization through response surface methodology (RSM) identified the optimal conditions (pH 9, 5 mg/L cephalexin, and 1.5 g/L catalyst dosage), under which degradation efficiencies of 73.4% (visible light) at 240 min and 96% (UV light) at 120 min were achieved. Under UV irradiation, both photolysis and photocatalytic degradation processes were carried out simultaneously, and this increases the degradation efficiency of cephalexin. Reusability results showed 4% reduction in cephalexin degradation after 5 runs. A pseudo-first-order kinetic model was obtained to photodegradation of cephalexin. Based on the trapping experiments, hydroxyl radicals are the main active species in the CEX photodegradation process.

## Data availability

The data supporting this study are available when reasonably requested from the corresponding author (MHZ).

Received: 20 December 2024; Accepted: 7 March 2025

Published online: 14 March 2025

## References

- Gordanshekan, A. et al. A comprehensive comparison of green Bi<sub>2</sub>WO<sub>6</sub>/gC<sub>3</sub>N<sub>4</sub> and Bi<sub>2</sub>WO<sub>6</sub>/TiO<sub>2</sub> S-scheme heterojunctions for photocatalytic adsorption/degradation of Cefixime: Artificial neural network, degradation pathway, and toxicity estimation. *Chem. Eng. J.* **451**, 139067 (2023).
- Rabanimehr, F. et al. Fabrication of Z-scheme Bi<sub>2</sub>WO<sub>6</sub>/CNT/TiO<sub>2</sub> heterostructure with enhanced cephalexin photodegradation: Optimization and reaction mechanism. *J. Mol. Liq.* **339**, 116728 (2021).
- Srivastava, S. K. Recent advances on removal of pharmaceuticals pollutants in wastewater using metal oxides and carbonaceous materials as photocatalysts: A review. *RSC Appl. Interfaces* **1**, 340–429 (2024).
- Karungamy, P. N. Methods used for removal of pharmaceuticals from wastewater: A review. *Appl. J. Environ. Eng. Sci.* **6**(4), 6–4 (2020).
- Yang, Y. et al. Efficient with low-cost removal and adsorption mechanisms of norfloxacin, ciprofloxacin and ofloxacin on modified thermal kaolin: Experimental and theoretical studies. *J. Hazard. Mater.* **430**, 128500 (2022).
- Duarte, A. C. et al. Antibiotic resistance in the drinking water: Old and new strategies to remove antibiotics, resistant bacteria, and resistance genes. *Pharmaceuticals* **15**(4), 393 (2022).
- Zangeneh, H. et al. Comparative study on photocatalytic performance of TiO<sub>2</sub> doped with different amino acids in degradation of antibiotics. *Water* **15**(3), 535 (2023).
- Benarab, N. & Fangninou, F. F. The issues of antibiotics: Cephalexin antibiotic as emerging environment contaminant. *Int. J. Sci. Res. Publ.* **10**(2), 306–318 (2020).
- Mohamed, A., Mahanna, H. & Samy, M. Synergistic effects of photocatalysis-periodate activation system for the degradation of emerging pollutants using GO/MgO nanohybrid. *J. Environ. Chem. Eng.* **12**(2), 112248 (2024).
- Alishiri, M. et al. Removal of ciprofloxacin and cephalexin antibiotics in water environment by magnetic graphene oxide nanocomposites; optimization using response surface methodology. *Results Eng.* **20**, 101507 (2023).



11. Rabanimehr, F., Farhadian, M. & Nazar, A. R. S. A high-performance microreactor integrated with chitosan/Bi<sub>2</sub>WO<sub>6</sub>/CNT/TiO<sub>2</sub> nanofibers for adsorptive/photocatalytic removal of cephalexin from aqueous solution. *Int. J. Biol. Macromol.* **208**, 260–274 (2022).
12. Lu, Z.-Y. et al. A critical review of antibiotic removal strategies: Performance and mechanisms. *J. Water Process Eng.* **38**, 101681 (2020).
13. Stancanelli, M. R. et al. Ogilvie syndrome and acute kidney injury: A rare complication of Cesarean section and preeclampsia. *J. Clin. Med.* **12**(6), 2249 (2023).
14. Borghei, S. A. et al. Synthesis of multi-application activated carbon from oak seeds by KOH activation for methylene blue adsorption and electrochemical supercapacitor electrode. *Arab. J. Chem.* **14**(2), 102958 (2021).
15. Zhu, L. et al. Synthesis of Ag-coated on a wrinkled SiO<sub>2</sub>@TiO<sub>2</sub> architectural photocatalyst: New method of wrinkled shell for use of semiconductors in the visible light range and penicillin antibiotic degradation. *Alex. Eng. J.* **61**(12), 9315–9334 (2022).
16. Yang, W. et al. Bio-originated mesosilicate SBA-15: Synthesis, characterization, and application for heavy metal removal. *NPJ Clean Water* **7**(1), 49 (2024).
17. Shirazian, S. et al. Economic nanobubbles by RFB and promoted PEF with yolk@ double-shell structural photocatalyst for degradation of pharmaceutical pollutants. *Npj Clean Water* **7**(1), 48 (2024).
18. Alibeigi-Beni, S. et al. Design and optimization of a hybrid process based on hollow-fiber membrane/coagulation for wastewater treatment. *Environ. Sci. Pollut. Res.* **28**, 8235–8245 (2021).
19. Habibi Zare, M. & Mehrabani-Zeinabad, A. Yolk@ Wrinkled-double shell smart nanoreactors: New platforms for mineralization of pharmaceutical wastewater. *Front. Chem.* **11**, 1211503 (2023).
20. Habibi Zare, M. & Mehrabani-Zeinabad, A. Rational design and synthesis of 3D nanoreactors for green fuel production: design band gap Y@ DS photocatalyst under visible irradiation. *ACS Appl. Energy Mater.* **6**(6), 3173–3199 (2023).
21. Marjani, A. et al. Synthesis of alginate-coated magnetic nanocatalyst containing high-performance integrated enzyme for phenol removal. *J. Environ. Chem. Eng.* **9**(1), 104884 (2021).
22. Rahmati, M. et al. Synthesis of Fe-TiO<sub>2</sub>/Al<sub>2</sub>O<sub>3</sub> nanocatalyst for photocatalytic reduction of nitrate ion from aqueous solution under visible light and UV irradiation. *Eur. Phys. J. Plus* **137**(7), 838 (2022).
23. Ali, N. S. et al. Performance of a solar photocatalysis reactor as pretreatment for wastewater via UV, UV/TiO<sub>2</sub>, and UV/H<sub>2</sub>O<sub>2</sub> to control membrane fouling. *Sci. Rep.* **12**(1), 16782 (2022).
24. Du, C. et al. A review of metal organic framework (MOFs)-based materials for antibiotics removal via adsorption and photocatalysis. *Chemosphere* **272**, 129501 (2021).
25. Vijayanand, M. et al. Polyaromatic hydrocarbons (PAHs) in the water environment: A review on toxicity, microbial biodegradation, systematic biological advancements, and environmental fate. *Environ. Res.* **227**, 115716 (2023).
26. Park, J. et al. Removal characteristics of pharmaceuticals and personal care products: Comparison between membrane bioreactor and various biological treatment processes. *Chemosphere* **179**, 347–358 (2017).
27. Askari, N. et al. Synthesis of CuWO<sub>4</sub>/Bi<sub>2</sub>S<sub>3</sub> Z-scheme heterojunction with enhanced Cephalexin photodegradation. *J. Photochem. Photobiol. A Chem.* **394**, 112463 (2020).
28. Mirhosseini, H. et al. Fabrication of an efficient ternary TiO<sub>2</sub>/Bi<sub>2</sub>WO<sub>6</sub> nanocomposite supported on g-C<sub>3</sub>N<sub>4</sub> with enhanced visible-light- photocatalytic activity: Modeling and systematic optimization procedure. *Arab. J. Chem.* **15**(4), 103729 (2022).
29. Zare, M. H. & Mehrabani-Zeinabad, A. Photocatalytic activity of ZrO<sub>2</sub>/TiO<sub>2</sub>/Fe<sub>3</sub>O<sub>4</sub> ternary nanocomposite for the degradation of naproxen: Characterization and optimization using response surface methodology. *Sci. Rep.* **12**(1), 10388 (2022).
30. Samy, M. et al. Solar-light-driven ZnO/biochar treatment of pesticides contaminated wastewater: A practical and computational study. *Energy Sci. Eng.* **10**(12), 4708–4725 (2022).
31. Abdel Azim, E. et al. Novel mint-stalks derived biochar for the adsorption of methylene blue dye: Effect of operating parameters, adsorption mechanism, kinetics, isotherms, and thermodynamics. *J. Environ. Manag.* **357**, 120738 (2024).
32. Mensah, K. et al. Rapid adsorption of sulfamethazine on mesoporous graphene produced from plastic waste: Optimization, mechanism, isotherms, kinetics, and thermodynamics. *Int. J. Environ. Sci. Technol.* **20**(9), 9717–9732 (2023).
33. Rani, B., Nayak, A. K. & Sahu, N. K. 1—Fundamentals principle of photocatalysis. In *Nanostructured Materials for Visible Light Photocatalysis* (eds Nayak, A. K. & Sahu, N. K.) 1–22 (Elsevier, 2022).
34. Rokesh, K., Sakar, M. & Do, T.-O. Emerging hybrid nanocomposite photocatalysts for the degradation of antibiotics: Insights into their designs and mechanisms. *Nanomaterials* **11**(3), 572 (2021).
35. Gaber, M. M. et al. Effective degradation of tetracycline and real pharmaceutical wastewater using novel nanocomposites of biosynthesized ZnO and carbonized toner powder. *Chemosphere* **352**, 141448 (2024).
36. Chen, D. et al. Photocatalytic degradation of organic pollutants using TiO<sub>2</sub>-based photocatalysts: A review. *J. Clean. Prod.* **268**, 121725 (2020).
37. Velepini, T., Prabakaran, E. & Pillay, K. Recent developments in the use of metal oxides for photocatalytic degradation of pharmaceutical pollutants in water—A review. *Mater. Today Chem.* **19**, 100380 (2021).
38. Prasad, C. et al. Recent advances in MXenes supported semiconductors based photocatalysts: Properties, synthesis and photocatalytic applications. *J. Ind. Eng. Chem.* **85**, 1–33 (2020).
39. Xue, Y. et al. Enhanced photocatalytic performance of iron oxides@ HTCC fabricated from zinc extraction tailings for methylene blue degradation: Investigation of the photocatalytic mechanism. *Int. J. Miner. Metall. Mater.* **30**(12), 2364–2374 (2023).
40. Ahmad, I. et al. Semiconductor photocatalysts: A critical review highlighting the various strategies to boost the photocatalytic performances for diverse applications. *Adv. Colloid Interface Sci.* **311**, 102830 (2023).
41. Kumar, S. G. & Devi, L. G. Review on modified TiO<sub>2</sub> photocatalysis under UV/visible light: Selected results and related mechanisms on interfacial charge carrier transfer dynamics. *J. Phys. Chem. A* **115**(46), 13211–13241 (2011).
42. Pelaez, M. et al. A review on the visible light active titanium dioxide photocatalysts for environmental applications. *Appl. Catal. B Environ.* **125**, 331–349 (2012).
43. Ahmadi, Y. & Kim, K.-H. Modification strategies for visible-light photocatalysts and their performance-enhancing effects on photocatalytic degradation of volatile organic compounds. *Renew. Sustain. Energy Rev.* **189**, 113948 (2024).
44. Basavarajappa, P. S. et al. Recent progress in metal-doped TiO<sub>2</sub>, non-metal doped/codoped TiO<sub>2</sub> and TiO<sub>2</sub> nanostructured hybrids for enhanced photocatalysis. *Int. J. Hydrog. Energy* **45**(13), 7764–7778 (2020).
45. Nur, A. S. et al. A review on the development of elemental and codoped TiO<sub>2</sub> photocatalysts for enhanced dye degradation under UV–vis irradiation. *J. Water Process Eng.* **47**, 102728 (2022).
46. Sukrey, N., Bushroa, A. & Rizwan, M. Dopant incorporation into TiO<sub>2</sub> semiconductor materials for optical, electronic, and physical property enhancement: Doping strategy and trend analysis. *J. Aust. Ceram. Soc.* **60**(2), 563–589 (2024).
47. Sultana, M. et al. Strategic development of metal doped TiO<sub>2</sub> photocatalysts for enhanced dye degradation activity under UV–Vis irradiation: A review. *Curr. Res. Green Sustain. Chem.* **7**, 100383 (2023).
48. Jonidi Jafari, A. & Moslemzadeh, M. Synthesis of Fe-doped TiO<sub>2</sub> for photocatalytic processes under UV-visible light: Effect of preparation methods on crystal size—A systematic review study. *Comments Inorg. Chem.* **40**(6), 327–346 (2020).
49. Fazilati, M. Photocatalytic degradation of amoxicillin, cephalexin, and tetracycline from aqueous solution: Comparison of efficiency in the usage of TiO<sub>2</sub>. *Desalin. Water Treat.* **169**, 222–231 (2019).
50. Rogé, V. et al. Improvement of the photocatalytic degradation property of atomic layer deposited ZnO thin films: The interplay between film properties and functional performances. *J. Mater. Chem. A* **3**(21), 11453–11461 (2015).
51. Aram, M. et al. Metronidazole and Cephalexin degradation by using of Urea/TiO<sub>2</sub>/ZnFe<sub>2</sub>O<sub>4</sub>/Clinoptilolite catalyst under visible-light irradiation and ozone injection. *J. Mol. Liq.* **304**, 112764 (2020).



52. Sood, S. et al. Highly effective Fe-doped TiO<sub>2</sub> nanoparticles photocatalysts for visible-light driven photocatalytic degradation of toxic organic compounds. *J. Colloid Interface Sci.* **450**, 213–223 (2015).
53. Yang, Y. et al. Doping and transformation mechanisms of Fe<sup>3+</sup> ions in Fe-doped TiO<sub>2</sub>. *CrystEngComm* **19**(7), 1100–1105 (2017).
54. Ellouzi, I. et al. Synthesis of Fe-doped TiO<sub>2</sub> with improved photocatalytic properties under Vis-L irradiation. *Iran. J. Catal.* **12**(3), 54 (2022).
55. Yuan, Y., Cui, J. & Zhang, F. Performance of iron-doped titanium dioxide-loaded activated carbon composite synthesized by simplified sol–gel method for ciprofloxacin degradation under ultraviolet light. *Water* **16**(12), 1739 (2024).
56. Rosa, D., Abbasova, N. & Di Palma, L. Titanium dioxide nanoparticles doped with iron for water treatment via photocatalysis: A review. *Nanomaterials* **14**(3), 293 (2024).
57. Ramirez, H. & Ramirez, M. *Photocatalytic Semiconductors: Synthesis, Characterization, and Environmental Applications* (Springer, 2015).
58. Wang, M. et al. Influence of calcination temperature on photocatalyst performances of floral Bi<sub>2</sub>O<sub>3</sub>/TiO<sub>2</sub> composite. *Catalysts* <https://doi.org/10.3390/catal12121635> (2022).
59. Sharma, S. et al. Solution combustion synthesized TiO<sub>2</sub>/Bi<sub>2</sub>O<sub>3</sub>/CuO nano-composites and their photocatalytic activity using visible LEDs assisted photoreactor. *Inorg. Chem. Commun.* **125**, 108418 (2021).
60. Sharma, S. et al. Mechanistic investigation of RhB photodegradation under low power visible LEDs using a Pd-modified TiO<sub>2</sub>/Bi<sub>2</sub>O<sub>3</sub> photocatalyst: Experimental and DFT studies. *J. Phys. Chem. Solids* **162**, 110510 (2022).
61. Mane, V. et al. A review on Bi<sub>2</sub>O<sub>3</sub> nanomaterial for photocatalytic and antibacterial applications. *Chem. Phys. Impact* **8**, 100517 (2024).
62. Wang, C. et al. Coherent Bi<sub>2</sub>O<sub>3</sub>–TiO<sub>2</sub> hetero-junction material through oriented growth as an efficient photo-catalyst for methyl orange degradation. *Mater. Today Chem.* **8**, 36–41 (2018).
63. Barahimi, V., Moghimi, H. & Taheri, R. A. Cu doped TiO<sub>2</sub>–Bi<sub>2</sub>O<sub>3</sub> nanocomposite for degradation of azo dye in aqueous solution: Process modeling and optimization using central composite design. *J. Environ. Chem. Eng.* **7**(3), 103078 (2019).
64. Wang, M. et al. Facile synthesis of nano-flower β-Bi<sub>2</sub>O<sub>3</sub>/TiO<sub>2</sub> heterojunction as photocatalyst for degradation RhB. *Molecules* **28**(2), 882 (2023).
65. Ruiz-Santoyo, V., García-Carvajal, S. & Arenas-Arrocena, M. C. Photocatalytic removal of synthetic dyes using Bi<sub>2</sub>O<sub>3</sub>–TiO<sub>2</sub> nanocomposites obtained by simple hydrothermal route. *J. Nanopart. Res.* **27**(2), 23 (2025).
66. Sood, S. et al. Bi<sub>2</sub>O<sub>3</sub>/TiO<sub>2</sub> heterostructures: Synthesis, characterization and their application in solar light mediated photocatalyzed degradation of an antibiotic, ofloxacin. *Chem. Eng. J.* **290**, 45–52 (2016).
67. Tolan, D. A. et al. Effect of bismuth doping on the crystal structure and photocatalytic activity of titanium oxide. *RSC Adv.* **13**(36), 25081–25092 (2023).
68. Al Marzouqi, F. et al. Thermal and hydrothermal synthesis of WO<sub>3</sub> nanostructure and its optical and photocatalytic properties for the degradation of Cephalexin and Nizatidine in aqueous solution. *Mater. Sci. Eng. B* **264**, 114991 (2021).
69. Eslami, A. et al. Optimization of sonochemical degradation of amoxicillin by sulfate radicals in aqueous solution using response surface methodology (RSM). *J. Mol. Liq.* **222**, 739–744 (2016).
70. Aydar, A. Y. Utilization of response surface methodology in optimization of extraction of plant materials. In *Statistical Approaches with Emphasis on Design of Experiments Applied to Chemical Processes* 157–169 (2018).
71. Ahadi, S., Moalej, N. S. & Sheibani, S. Characteristics and photocatalytic behavior of Fe and Cu doped TiO<sub>2</sub> prepared by combined sol-gel and mechanical alloying. *Solid State Sci.* **96**, 105975 (2019).
72. Khan, M. S. et al. Synthesis and characterization of Fe–TiO<sub>2</sub> nanomaterial: performance evaluation for RB5 decolorization and in vitro antibacterial studies. *Nanomaterials* **11**(2), 436 (2021).
73. Moradi, V. et al. Acid-treated Fe-doped TiO<sub>2</sub> as a high performance photocatalyst used for degradation of phenol under visible light irradiation. *J. Environ. Sci.* **83**, 183–194 (2019).
74. Yadav, H. M. et al. Enhanced photocatalytic inactivation of bacteria on Fe-containing TiO<sub>2</sub> nanoparticles under fluorescent light. *J. Mater. Sci. Mater. Med.* **27**, 1–9 (2016).
75. Kusumawardani, L. & Syahputri, Y. Study of structural and optical properties of Fe (III)-doped TiO<sub>2</sub> prepared by sol-gel method. In *IOP Conference Series: Earth and Environmental Science*. (IOP Publishing, 2019).
76. Cřišan, M. et al. Sol–gel iron-doped TiO<sub>2</sub> nanopowders with photocatalytic activity. *Appl. Catal. A Gen.* **504**, 130–142 (2015).
77. Eskandari, P. et al. Adsorption and photodegradation efficiency of TiO<sub>2</sub>/Fe<sub>2</sub>O<sub>3</sub>/PAC and TiO<sub>2</sub>/Fe<sub>2</sub>O<sub>3</sub>/zeolite nanophotocatalysts for the removal of cyanide. *Ind. Eng. Chem. Res.* **58**(5), 2099–2112 (2019).
78. Eshaghi, A. & Moradi, H. Optical and photocatalytic properties of the Fe-doped TiO<sub>2</sub> nanoparticles loaded on the activated carbon. *Adv. Powder Technol.* **29**(8), 1879–1885 (2018).
79. Khan, H. & Swati, I. K. Fe<sup>3+</sup>-doped anatase TiO<sub>2</sub> with d–d transition, oxygen vacancies and Ti<sup>3+</sup> centers: Synthesis, characterization, UV–vis photocatalytic and mechanistic studies. *Ind. Eng. Chem. Res.* **55**(23), 6619–6633 (2016).
80. Wang, M. et al. Influence of calcination temperature on photocatalyst performances of floral Bi<sub>2</sub>O<sub>3</sub>/TiO<sub>2</sub> composite. *Catalysts* **12**(12), 1635 (2022).
81. Liu, Y. et al. Synthesis, characterization, and activities of visible light-driven Bi<sub>2</sub>O<sub>3</sub>–TiO<sub>2</sub> composite photocatalysts. *J. Alloys Compd.* **498**(2), 179–184 (2010).
82. Cynthia, S. & Sagadevan, S. Physicochemical and magnetic properties of pure and Fe doped TiO<sub>2</sub> nanoparticles synthesized by sol–gel method. *Mater. Today Proc.* **50**, 2720–2724 (2022).
83. Yalçın, Y., Kılıç, M. & Çınar, Z. Fe<sup>3+</sup>-doped TiO<sub>2</sub>: A combined experimental and computational approach to the evaluation of visible light activity. *Appl. Catal. B Environ.* **99**(3–4), 469–477 (2010).
84. Ali, T. et al. Photocatalytic performance of Fe-doped TiO<sub>2</sub> nanoparticles under visible-light irradiation. *Mater. Res. Express* **4**(1), 015022 (2017).
85. Komaraiah, D. et al. Structural, optical and photoluminescence studies of sol–gel synthesized pure and iron doped TiO<sub>2</sub> photocatalysts. *Ceram. Int.* **45**(18), 25060–25068 (2019).
86. An, L. et al. Ultrasonic-assisted synthesis of visible-light-driven TiO<sub>2</sub>/Bi<sub>2</sub>O<sub>3</sub> nanocomposite photocatalysts: Characterization, properties and azo dye removal application. *Res. Chem. Intermed.* **41**, 7449–7461 (2015).
87. Zeng, G. et al. Preparation of TiO<sub>2</sub> and Fe–TiO<sub>2</sub> with an impinging stream-rotating packed bed by the precipitation method for the photodegradation of gaseous toluene. *Nanomaterials* **9**(8), 1173 (2019).
88. Yu, J., Xiang, Q. & Zhou, M. Preparation, characterization and visible-light-driven photocatalytic activity of Fe-doped titania nanorods and first-principles study for electronic structures. *Appl. Catal. B Environ.* **90**(3–4), 595–602 (2009).
89. Reddy, N. L. et al. Highly efficient hydrogen production using Bi<sub>2</sub>O<sub>3</sub>/TiO<sub>2</sub> nanostructured photocatalysts under led light irradiation. *Mater. Today Proc.* **3**(6), 1351–1358 (2016).
90. Barkhade, T. & Banerjee, I. Photocatalytic degradation of Rhodamine B dye using Fe doped TiO<sub>2</sub> nanocomposites. In *AIP Conference Proceedings*. (AIP Publishing, 2018).
91. Mironyuk, I. et al. Photocatalytic degradation of Congo red dye using Fe-doped TiO<sub>2</sub> nanocatalysts. *Phys. Chem. Solid State* **22**(4), 697–710 (2021).
92. Barkhade, T. & Banerjee, I. Optical properties of Fe doped TiO<sub>2</sub> nanocomposites synthesized by sol–gel technique. *Mater. Today Proc.* **18**, 1204–1209 (2019).
93. Gillard, J. *A First Course in Statistical Inference* (Springer, 2020).
94. Kumar, K. V., Porkodi, K. & Rocha, S. Langmuir–Hinshelwood kinetics—A theoretical study. *Catal. Commun.* **9**(1), 82–84 (2008).

95. Toriki, F. & Faghihian, H. Sunlight-assisted decomposition of cephalexin by novel synthesized NiS-PPY-Fe<sub>3</sub>O<sub>4</sub> nanophotocatalyst. *J. Photochem. Photobiol. A Chem.* **338**, 49–59 (2017).
96. Ajoudanian, N. & Nezamzadeh-Ejhi, A. Enhanced photocatalytic activity of nickel oxide supported on clinoptilolite nanoparticles for the photodegradation of aqueous cephalexin. *Mater. Sci. Semicond. Process.* **36**, 162–169 (2015).
97. Azimi, S. & Nezamzadeh-Ejhi, A. Enhanced activity of clinoptilolite-supported hybridized PbS–CdS semiconductors for the photocatalytic degradation of a mixture of tetracycline and cephalexin aqueous solution. *J. Mol. Catal. A Chem.* **408**, 152–160 (2015).
98. Fazilati, M., Hassani, A. & Torabian, A. Photocatalytic degradation of amoxicillin and cephalexin from aqueous solution by ZnO and TiO<sub>2</sub>. In *International Congress on Engineering Science and Sustainable Urban Development Denmark* (2018).

## Author contributions

Zeynab Abdeyazdan: Conceptualization, Formal analysis, Investigation, Writing—Original Draft, Visualization, Arjomand Mehrabani-Zeinabad: Conceptualization, Formal analysis, Investigation, Writing—Original Draft, Visualization, Mohammad Rahmati: Conceptualization, Formal analysis, Investigation, Writing—Original Draft, Visualization, Masoud Habibi Zare: Conceptualization, Formal analysis, Investigation, Writing—Original Draft, Visualization.

## Declarations

### Competing interests

The authors declare no competing interests.

### Additional information

**Correspondence** and requests for materials should be addressed to M.H.Z.

**Reprints and permissions information** is available at [www.nature.com/reprints](http://www.nature.com/reprints).

**Publisher's note** Springer Nature remains neutral with regard to jurisdictional claims in published maps and institutional affiliations.

**Open Access** This article is licensed under a Creative Commons Attribution-NonCommercial-NoDerivatives 4.0 International License, which permits any non-commercial use, sharing, distribution and reproduction in any medium or format, as long as you give appropriate credit to the original author(s) and the source, provide a link to the Creative Commons licence, and indicate if you modified the licensed material. You do not have permission under this licence to share adapted material derived from this article or parts of it. The images or other third party material in this article are included in the article's Creative Commons licence, unless indicated otherwise in a credit line to the material. If material is not included in the article's Creative Commons licence and your intended use is not permitted by statutory regulation or exceeds the permitted use, you will need to obtain permission directly from the copyright holder. To view a copy of this licence, visit <http://creativecommons.org/licenses/by-nc-nd/4.0/>.

© The Author(s) 2025